

1 **The new Kr-86 excess ice core proxy for synoptic activity: West Antarctic**
2 **storminess possibly linked to ITCZ movement through the last deglaciation**

3 Christo Buizert¹, Sarah Shackleton², Jeffrey P. Severinghaus², William H. G. Roberts³, Alan Seltzer^{2,4},
4 Bernhard Bereiter⁵, Kenji Kawamura⁶, Daniel Baggenstos⁵, Anaïs J. Orsi^{7,8}, Ikumi Oyabu⁶,
5 Benjamin Birner², Jacob D. Morgan², Edward J. Brook¹, David M. Etheridge^{9,10}, David Thornton^{9,10},
6 Nancy Bertler^{11,12}, Rebecca L. Pyne¹¹, Robert Mulvaney¹³, Ellen Mosley-Thompson¹⁴, Peter D. Neff^{15,16},
7 and Vasilii V. Petrenko¹⁶

8 ¹College of Earth, Ocean and Atmospheric Sciences, Oregon State University, Corvallis, OR 97331, USA

9 ²Scripps Institution of Oceanography, University of California San Diego, La Jolla, CA 92093, USA

10 ³Geography and Environmental Sciences, Northumbria University, Newcastle, UK and BRIDGE, School
11 of Geographical Sciences, University of Bristol, Bristol, UK

12 ⁴Marine Chemistry and Geochemistry Department, Woods Hole Oceanographic Institution, Woods Hole,
13 MA 02543, USA

14 ⁵Climate and Environmental Physics, Physics Institute, and Oeschger Center for Climate Research,
15 University of Bern, 3012, Bern, Switzerland

16 ⁶National Institute for Polar Research, 10-3 Midori-cho, Tachikawa, Tokyo 190-8518, Japan

17 ⁷Laboratoire des Sciences du Climat et de l'Environnement, LSCE/IPSL, CEA-CNRS-UVSQ, Université
18 Paris-Saclay, l'Orme des merisiers, Gif-sur-Yvette, France

19 ⁸Earth, Ocean and Atmospheric Sciences Department, The University of British Columbia, Vancouver, BC
20 V6T 1Z4, Canada

21 ⁹CSIRO Environment, PMB 1, Aspendale, Victoria 3195, Australia

22 ¹⁰Australian Antarctic Program Partnership, Institute for Marine & Antarctic Studies, University of
23 Tasmania, Hobart, Tasmania 7004, Australia

24 ¹¹Antarctic Research Centre, Victoria University of Wellington, Wellington, 6012, New Zealand

25 ¹²GNS Science, Lower Hut 5010, New Zealand

26 ¹³British Antarctic Survey, National Environment Research Council, Cambridge CB3 0ET, UK

27 ¹⁴Byrd Polar and Climate Research Center, The Ohio State University, Columbus, OH 43210, USA

28 ¹⁵Department of Soil, Water, and Climate, University of Minnesota, Saint Paul, MN 55108, USA

29 ¹⁶Department of Earth and Environmental Sciences, University of Rochester, Rochester, NY 14627, USA
30

31 *Correspondence to:* Christo Buizert (christo.buizert@oregonstate.edu)

32 **Abstract**

33 Here we present a newly developed ice core gas-phase proxy that directly samples a component of the
34 large-scale atmospheric circulation: synoptic-scale pressure variability. Surface pressure changes weakly
35 disrupt gravitational isotopic settling in the firn layer, which is recorded in krypton-86 excess ($^{86}\text{Kr}_{\text{xs}}$). The
36 $^{86}\text{Kr}_{\text{xs}}$ reflects the time-averaged synoptic pressure variability over several years (site “storminess”), and
37 does not record individual synoptic events. We validate $^{86}\text{Kr}_{\text{xs}}$ using late Holocene ice samples from eleven
38 Antarctic and one Greenland ice core that collectively represent a wide range of surface pressure variability
39 in the modern climate. We find a strong spatial correlation ($r = -0.94$, $p < 0.01$) between site-average $^{86}\text{Kr}_{\text{xs}}$
40 and time-averaged synoptic variability from reanalysis data. The main uncertainties in the analysis are the
41 corrections for gas loss and thermal fractionation, and the relatively large scatter in the data. Limited
42 scientific understanding of the firn physics and potential biases of $^{86}\text{Kr}_{\text{xs}}$ require caution in interpreting this
43 proxy at present. We show Antarctic $^{86}\text{Kr}_{\text{xs}}$ is linked to the position of the southern hemisphere eddy-driven
44 subpolar jet (SPJ), with a southern position enhancing pressure variability.

45 We present a $^{86}\text{Kr}_{\text{xs}}$ record covering the last 24 ka from the WAIS Divide ice core. West Antarctic synoptic
46 activity is slightly below modern levels during the last glacial maximum (LGM); increases during the
47 Heinrich Stadial 1 and Younger Dryas North Atlantic cold periods; weakens abruptly at the Holocene onset;
48 remains low during the early and mid-Holocene, and gradually increases to its modern value. The WAIS
49 Divide $^{86}\text{Kr}_{\text{xs}}$ record resembles records of monsoon intensity thought to reflect changes in the meridional
50 position of the intertropical convergence zone (ITCZ) on orbital and millennial timescales, such that West
51 Antarctic storminess is weaker when the ITCZ is displaced northward, and stronger when it is displaced
52 southward. We interpret variations in synoptic activity as reflecting movement of the South Pacific SPJ in
53 parallel to the ITCZ migrations, which is the expected zonal-mean response of the eddy-driven jet in models
54 and proxy data. Past changes to Pacific climate and the El Niño Southern Oscillation (ENSO) may amplify
55 the signal of the SPJ migration. Our interpretation is broadly consistent with opal flux records from the
56 Pacific Antarctic zone thought to reflect wind-driven upwelling.

57 We emphasize that $^{86}\text{Kr}_{\text{xs}}$ is a new proxy, and more work is called for to confirm, replicate and better
58 understand these results; until such time, our conclusions regarding past atmospheric dynamics remain
59 speculative. Current scientific understanding of firn air transport and trapping is insufficient to explain all
60 the observed variations in $^{86}\text{Kr}_{\text{xs}}$. A list of suggested future studies is provided.

61 **1 Introduction**

62 **1.1 Motivation and objectives**

63 Proxy records from around the globe show strong evidence for past changes in Earth's atmospheric
64 circulation and hydrological cycle that often far exceed those seen in the relatively short instrumental
65 period.

66 For example, low-latitude records of riverine discharge captured in ocean sediments (Peterson et al., 2000),
67 and isotopic composition of meteoric water captured in dripstone calcite (Cheng et al., 2016), suggest large
68 variations in tropical hydrology and monsoon strength, commonly interpreted as meridional migrations of
69 the intertropical convergence zone or ITCZ (Chiang and Friedman, 2012; Schneider et al., 2014). Such
70 ITCZ movement is seen both in response to insolation changes linked to planetary orbit (Cruz et al., 2005)
71 as well as in response to the abrupt millennial-scale Dansgaard-Oeschger (D-O) and Heinrich cycles of the
72 North-Atlantic (Kanner et al., 2012; Wang et al., 2001); the organizing principle is that the ITCZ follows
73 the thermal equator and therefore migrates towards the warmer (or warming) hemisphere (Broccoli et al.,
74 2006; Chiang and Bitz, 2005).

75 As a second example, the intensity of the El Niño – Southern Oscillation (ENSO), the dominant mode of
76 global interannual climate variability, has changed through time. A variety of proxy data suggest ENSO
77 activity in the 20th century was much stronger than in preceding centuries (Emile-Geay et al., 2015; Fowler
78 et al., 2012; Gergis and Fowler, 2009; Thompson et al., 2013). The vast majority of data and model studies
79 suggest weakened ENSO strength in the mid- and early-Holocene, likely in response to stronger orbitally-
80 driven NH summer insolation at that time (Braconnot et al., 2012; Cane, 2005; Clement et al., 2000; Driscoll
81 et al., 2014; Koutavas et al., 2006; Liu et al., 2000; Liu et al., 2014; Moy et al., 2002; Rein et al., 2005;
82 Tudhope et al., 2001; Zheng et al., 2008); yet other studies suggest there may not be such a clear trend, and
83 simply more variability (Cobb et al., 2013). Intensification of ENSO (or perhaps a more El-Niño-like mean
84 state) may have occurred during the North-Atlantic cold phases of the abrupt D-O and Heinrich cycles
85 (Braconnot et al., 2012; Merkel et al., 2010; Stott et al., 2002; Timmermann et al., 2007). Overall,
86 understanding past and future ENSO variability remains extremely challenging (Cai et al., 2015).

87 As a last example, the strength and meridional position of the southern hemisphere westerlies (SHW) is
88 thought to have changed in the past, which, via Southern Ocean wind-driven upwelling, has potential
89 implications for the global overturning circulation (Marshall and Speer, 2012) and for carbon storage in the
90 abyssal ocean (Anderson et al., 2009; Russell et al., 2006; Toggweiler et al., 2006). The SHW are thought
91 to be shifted equatorward (Kohfeld et al., 2013) during the last glacial maximum (LGM), a shift on which
92 climate models disagree (Rojas et al., 2009; Sime et al., 2013). During the abrupt D-O and Heinrich cycles,
93 the SHW move in parallel with the aforementioned migrations of the ITCZ in both data (Buizert et al.,
94 2018; Marino et al., 2013; Markle et al., 2017) and models (Lee et al., 2011; Pedro et al., 2018; Rind et al.,
95 2001).

96 As these examples clearly illustrate, evidence of past changes to the large-scale atmospheric circulation is
97 widespread. However, proxy evidence of such past changes is typically indirect – for example via isotopes
98 in precipitation, sea surface temperature, ocean frontal positions, windblown dust, or ocean upwelling –
99 complicating their interpretation. Here we present a newly developed noble gas-based ice core proxy, Kr-

100 $^{86}\text{Kr}_{\text{xs}}$), that directly samples a component of the large-scale atmospheric circulation: synoptic-
 101 scale pressure variability. Owing to the firm air residence time of several years (Buizert et al., 2013) and the
 102 gradual bubble trapping process, each ice core sample contains a distribution of gas ages, rather than a
 103 single age. Therefore, $^{86}\text{Kr}_{\text{xs}}$ does not record the passing of individual weather systems, but rather the time-
 104 average intensity of synoptic-scale barometric variability.

105 Here we provide the first complete description of this new proxy. We validate and calibrate $^{86}\text{Kr}_{\text{xs}}$ using
 106 late-Holocene ice core samples from locations around Antarctica and Greenland that represent a wide range
 107 of pressure variability in the modern climate. We discuss the difficulties in using this proxy (analytical
 108 precision, surface melt, corrections for sample gas loss and thermal fractionation). Next, we use reanalysis
 109 data to better understand the drivers of surface pressure variability in Antarctica. Last, we present an $^{86}\text{Kr}_{\text{xs}}$
 110 records from the Antarctic WAIS Divide ice core through the last deglaciation.

111 **1.2 Gravitational disequilibrium and Kr-86 excess**

112 The upper 50-100 m of the ice sheet accumulation zone consists of firm, the unconsolidated intermediate
 113 stage between snow and ice. An interconnected pore network exists within the firm, in which gas transport
 114 is dominated by molecular diffusion (Schwander et al., 1993). Diffusion in this stagnant air column results
 115 in gravitational enrichment in heavy gas isotopic ratios such as $\delta^{15/14}\text{N-N}_2$, $\delta^{40/36}\text{Ar}$ and $\delta^{86/82}\text{Kr}$ (Schwander,
 116 1989; Sowers et al., 1992). In gravitational equilibrium, all these gases attain the same degree of isotopic
 117 enrichment per unit mass difference:

$$118 \quad \delta_{\text{grav}}(z) = \left[\exp\left(\frac{\Delta m g z}{RT}\right) - 1 \right] \times 1000\text{‰} \quad (1)$$

119 with Δm the isotopic mass difference ($1 \times 10^{-3} \text{ kg mol}^{-1}$), g the gravitational acceleration, z the depth, R the
 120 gas constant and T the Kelvin temperature.

121 Besides molecular diffusion, firm air is mixed and transported via three other processes: downward
 122 advection with the sinking ice matrix, convective mixing (used in the firm air literature as an umbrella term
 123 to denote vigorous air exchange with the atmosphere via e.g. wind pumping and seasonal convection), and
 124 dispersive mixing. These last three transport processes are all driven by large-scale air movement that does
 125 not distinguish between isotopologues, and we refer to them collectively as macroscopic air movement. Of
 126 particular interest for our proxy is dispersive mixing, which is driven by surface pressure variations. When
 127 a low-pressure (high-pressure) system moves into the site, firm air at all depth levels is forced upwards
 128 (downwards) to reach hydrostatic equilibrium with the atmosphere – a process called barometric pumping.
 129 One can think of the firm layer “breathing” in and out in response to a rising and falling barometer,
 130 respectively. Because firm has a finite dispersivity (Schwander et al., 1988), this air movement mixes the
 131 interstitial firm air (Buizert and Severinghaus, 2016). The upward air flow due to gradual pore closure is
 132 orders of magnitude smaller than the flows driven via barometric pumping, and neglected here.

133 Any type of macroscopic air movement disturbs the gravitational settling, reducing isotopic enrichment
 134 below δ_{grav} . Let $\delta^{86}\text{Kr}$, $\delta^{40}\text{Ar}$, and $\delta^{15}\text{N}$ refer to deviations of $^{86}\text{Kr}/^{82}\text{Kr}$, $^{40}\text{Ar}/^{36}\text{Ar}$, and $^{29}\text{N}_2/^{28}\text{N}_2$, respectively,
 135 from their ratios in the well-mixed atmosphere. Gases that diffuse faster (such as N_2) will always be closer
 136 to gravitational equilibrium than gases that diffuse slower (such as Kr), and in the absence of thermal
 137 fractionation $\delta^{86}\text{Kr}/4 < \delta^{40}\text{Ar}/4 < \delta^{15}\text{N} < \delta_{\text{grav}}$. The isotopic differences $\delta^{86}\text{Kr}/4 - \delta^{40}\text{Ar}/4$ and $\delta^{86}\text{Kr}/4 - \delta^{15}\text{N}$

138 thus reflect the degree of gravitational disequilibrium. The magnitudes of the isotopic disequilibria scale in
 139 a predictable way following the molecular diffusion coefficients (Birner et al., 2018); because the diffusion
 140 coefficients of N₂ and Ar are very similar, their disequilibria are comparable in magnitude. We define Kr-
 141 86 excess using the Kr and Ar isotopic difference:

$$142 \quad {}^{86}\text{Kr}_{\text{xs}40} = \frac{\delta^{86}\text{Kr}_{\text{corr}} - \delta^{40}\text{Ar}_{\text{corr}}}{\delta^{40}\text{Ar}_{\text{corr}}} \times 1000 \text{ per meg } \text{‰}^{-1} \quad (2)$$

143 where the “corr” subscript denotes a correction for gas loss (Appendix A1) and thermal fractionation
 144 (Appendix A2). The rationale for including a normalization in the denominator is discussed below. An
 145 alternative Kr-86 excess definition is possible using $\delta^{15}\text{N}$ instead of $\delta^{40}\text{Ar}$:

$$146 \quad {}^{86}\text{Kr}_{\text{xs}15} = \frac{\delta^{86}\text{Kr}_{\text{corr}/4} - \delta^{15}\text{N}_{\text{corr}}}{\delta^{15}\text{N}_{\text{corr}}} \times 1000 \text{ per meg } \text{‰}^{-1} \quad (3)$$

147 Note that both definitions rely on having measurements of three isotope ratios ($\delta^{86}\text{Kr}$, $\delta^{40}\text{Ar}$ and $\delta^{15}\text{N}$), as
 148 the thermal correction requires $\delta^{40}\text{Ar}$ and $\delta^{15}\text{N}$ be known. The ${}^{86}\text{Kr}_{\text{xs}40}$ definition is preferred, because per
 149 unit mass difference $\delta^{40}\text{Ar}$ is less sensitive to thermal fractionation than $\delta^{15}\text{N}$ is (Grachev and Severinghaus,
 150 2003a; 2003b); this makes it more suitable for interpreting time series. Unless explicitly stated otherwise,
 151 we use ${}^{86}\text{Kr}_{\text{xs}40}$ as our definition of Kr-86 excess. The ${}^{86}\text{Kr}_{\text{xs}15}$ does provide a way to check the validity of
 152 ${}^{86}\text{Kr}_{\text{xs}40}$ timeseries, and indeed we find good correspondence between both definitions for the WDC
 153 deglacial timeseries. Because the disequilibrium signal is small, we express ${}^{86}\text{Kr}_{\text{xs}}$ in units of per meg (parts
 154 per million) of gravitational disequilibrium per ‰ of gravitational enrichment. This unit (per meg ‰⁻¹) is
 155 mathematically identical to ‰, but we use it to emphasize the normalization in the denominator.

156 In the (theoretical) case of full gravitational equilibrium (and no gas loss or thermal fractionation), $\delta^{86}\text{Kr}/4$
 157 = $\delta^{40}\text{Ar}/4 = \delta^{15}\text{N} = \delta_{\text{grav}}$, and therefore ${}^{86}\text{Kr}_{\text{xs}} = 0$. Any type of macroscopic mixing will cause $\delta^{86}\text{Kr}/4 <$
 158 $\delta^{40}\text{Ar}/4 < \delta^{15}\text{N} < \delta_{\text{grav}}$, and thus ${}^{86}\text{Kr}_{\text{xs}} < 0$. In this sense ${}^{86}\text{Kr}_{\text{xs}}$ is a quantitative measure for the degree of
 159 gravitational disequilibrium in the firn layer (Birner et al., 2018; Buizert and Severinghaus, 2016).

160 Kawamura et al. (2013) first describe this gravitational disequilibrium (or kinetic) fractionation effect at
 161 the Megadunes site (Severinghaus et al., 2010), where deep firn cracking leads to a 23 m-thick convective
 162 zone. They suggest that the isotopic disequilibrium can be used to estimate past convective zone thickness.
 163 We show here that sites with small convective zones can nevertheless have very negative ${}^{86}\text{Kr}_{\text{xs}}$, and instead
 164 we suggest that the ice core ${}^{86}\text{Kr}_{\text{xs}}$ is dominated by dispersive mixing driven by barometric pumping from
 165 time-averaged synoptic-scale pressure variability.

166 The principle behind ${}^{86}\text{Kr}_{\text{xs}}$ is illustrated with idealized firn model experiments in Fig. 1. In the absence of
 167 dispersive mixing (Fig. 1A, left panel), all isotope ratios approach δ_{grav} and $\delta^{86}\text{Kr} - \delta^{40}\text{Ar}$ is close to zero –
 168 but not exactly zero owing to downward air advection. Next, we replace a fraction f of the molecular
 169 diffusion with dispersive mixing. With dispersive mixing at $f=0.1$ and $f=0.2$ of total mixing (middle and

170 right panels, respectively), isotopic enrichment is progressively reduced below δ_{grav} (dashed line), making
171 $\delta^{86}\text{Kr} - \delta^{40}\text{Ar}$ (and consequently $^{86}\text{Kr}_{\text{xs}}$) increasingly negative.

172 The ratio of macroscopic over diffusive transport is expressed via the dimensionless Péclet number, given
173 here for advection and dispersion:

$$174 \quad \text{Pe}_X = \frac{w_{\text{air}}L + D_{\text{disp}}}{D_X} \quad (4)$$

175 where Pe_X is the Péclet number for gas X , w_{air} the (downward) advective air velocity, L a characteristic
176 length scale, D_X the diffusion coefficient for gas X , and D_{disp} is the dispersion coefficient (Buizert and
177 Severinghaus, 2016). In agreement with earlier studies (Birner et al., 2018; Kawamura et al., 2013), we find
178 that $\delta^{86}\text{Kr} - \delta^{40}\text{Ar}$ is maximized when molecular and dispersive mixing are equal in magnitude ($f = 0.5$, Fig.
179 1B), corresponding to $\text{Pe}_X \approx 1$. Note that $^{86}\text{Kr}_{\text{xs}}$ responds more linearly to f than $\delta^{86}\text{Kr} - \delta^{40}\text{Ar}$ does, due to
180 $\delta^{40}\text{Ar}$ in the denominator of Eq. (2).

181 In a last idealized experiment, we keep the fraction of dispersion fixed at $f = 0.1$ while we reduce the
182 thickness of the firn column by increasing the site temperature (Fig. 1C). We find that $\delta^{86}\text{Kr} - \delta^{40}\text{Ar}$ scales
183 linearly with firn thickness, here represented by $\delta^{40}\text{Ar}$ on the x-axis. However, $^{86}\text{Kr}_{\text{xs}}$ remains essentially
184 constant due to the normalization by $\delta^{40}\text{Ar}$ in the denominator of Eq. (2). The normalization step is thus
185 necessary to enable meaningful comparison between different sites and time periods that all have different
186 firn thicknesses. For this reason, the definition of $^{86}\text{Kr}_{\text{xs}}$ used here has been updated from the original
187 definition by (Buizert and Severinghaus, 2016).

188 Note that these highly idealized experiments assume dispersive mixing to be a fixed fraction of total
189 transport throughout the firn column, equivalent to a constant Péclet number in the diffusive zone (a
190 convective zone is absent in these simulations). In reality, the Péclet number varies greatly on all spatial
191 scales. On the macroscopic scale (> 1 m), Pe reflects the various transport regimes (Sowers et al., 1992),
192 being highest in the convective and lock-in zones. On the microscopic scale (< 1 cm), hydraulic
193 conductance scales as $\propto r^4$ (with r the pore radius) whereas the diffusive conductance scales as $\propto r^2$. This
194 means that the Darcy flow associated with barometric pumping will concentrate in the widest pores and
195 pathways, leading to a range of effective Péclet numbers within a single sample of firn. At intermediate
196 spatial scales of a few cm, firn density layering introduces strong heterogeneity in transport properties. It is
197 unclear at present whether the competition between diffusive and non-diffusive transport, which occurs at
198 the microscopic pore level, can be accurately represented in macroscopic firn air models via a linear
199 parameterization as is the current practice.

200

201 **2 Methods**

202 **2.1 Ice core sites**

203 In this study we use ice samples from eleven ice cores drilled in Antarctica, and one in Greenland. The
204 Antarctic sites are: West Antarctic Ice Sheet (WAIS) Divide core (WDC06A, or WDC), Siple Dome
205 (SDM), James Ross Island (JRI), Bruce Plateau (BRP), Law Dome DE08, Law Dome DE08-OH, Law
206 Dome DSSW20K, Roosevelt Island Climate Evolution (RICE), Dome Fuji (DF), EPICA (European Project
207 for Ice Coring in Antarctica) Dome C (EDC), and South Pole Ice Core (SPC14, or SP). Ice core locations
208 in Antarctica are shown in Fig. 2A. In Greenland, we use samples from the Greenland Ice Sheet Project 2
209 (GISP2).

210 We shall refer to late Holocene data from these sites as the calibration dataset, analogous to a core top data
211 set in the sediment coring literature. Site characteristics, coordinates, and number of samples included in
212 the calibration data set are given in Table 1. The DE08-OH site is a recent revisit of the Law Dome DE08
213 site. The DE08-OH core was measured at sub-annual resolution to understand cm-scale $^{86}\text{Kr}_{\text{xs}}$ variations
214 due to for example layering in firn density and bubble trapping (Appendix B). In addition to the calibration
215 data set, we present a record of Kr-86 excess going back to the LGM from WDC.

216 **2.2 Ice sample analysis**

217 We broadly follow analytical procedures described elsewhere (Bereiter et al., 2018a; Bereiter et al., 2018b;
218 Headly and Severinghaus, 2007; Severinghaus et al., 2003). In short, an 800 g ice sample, its edges trimmed
219 with a band saw to expose fresh surfaces, is placed in a chilled vacuum flask that is then evacuated for 20
220 minutes using a turbomolecular pump. Air is extracted from the ice by melting the sample while stirring
221 vigorously with a magnetic stir bar, led through a water trap, and cryogenically trapped in a dip tube
222 immersed in liquid He. Next, the sample is split into two unequal fractions. The smaller fraction (about 2%
223 of total air) is analyzed for $\delta^{15}\text{N-N}_2$, $\delta^{18}\text{O-O}_2$, $\delta\text{O}_2/\text{N}_2$ and $\delta\text{Ar}/\text{N}_2$ on a 3kV Thermo Finnigan Delta V plus
224 dual inlet IRMS (isotope ratio mass spectrometer). In the larger fraction, noble gases are isolated via hot
225 gettering to remove reactive gases. The purified noble gases are then analyzed for $\delta^{40/36}\text{Ar}$, $\delta^{40/38}\text{Ar}$, $\delta^{86/82}\text{Kr}$,
226 $\delta^{86/84}\text{Kr}$, $\delta^{86/83}\text{Kr}$, $\delta\text{Kr}/\text{Ar}$ and $\delta\text{Xe}/\text{Ar}$ on a 10kV Thermo Finnigan MAT253 dual inlet IRMS. We reject
227 one sample from RICE due to incomplete sample transfer, and one sample from WDC due to problems
228 with the water trap. Calibration is done for each measurement campaign by running samples of La Jolla
229 pier air.

230 All calibration (core top) data were measured using “Method 2” as described by Bereiter et al. (2018a),
231 with a longer equilibration time during the splitting step than used in that study to improve isotopic
232 equilibration between the fractions. The exception is the DE08-OH site, where the ice sample (rather than
233 the extracted gas sample) was split into two fractions – the advantage of this approach is that it does not
234 require a gas splitting step that is time-consuming and may fractionate the isotopes; the downside is that
235 the samples may have slightly different isotopic composition due to the stochastic nature of bubble trapping
236 and the different gas-loss histories of the ice pieces.

237 Measurements of the WDC downcore data set were performed over five separate measurement campaigns
238 that occurred in February-April 2014, February-April 2015, August 2015, August 2020, and August 2021,

239 respectively. The first three campaigns are described by Bereiter et al. (2018b), in which the $^{86}\text{Kr}_{\text{xs}}$ data are
240 a by-product of measuring $\delta\text{Kr}/\text{N}_2$ for reconstructing global mean ocean temperature. Campaigns 1 and 2
241 are in good agreement, whereas campaign 3 appears offset from the other two by an amount that exceeds
242 the analytical precision (offset around 35 per meg ‰^{-1}). To validate the main features in the record, we
243 performed two additional campaigns (4 and 5), in which all the gas extracted from each ice sample was
244 quantitatively gettered and only analysed for Ar and Kr isotopic composition. The downcore record, as well
245 as the five analytical campaigns, are discussed in detail in section 5.1. Data from the bubble-clathrate
246 transition zone (here 1000 to 1600 m depth, or $\sim 4\text{ka}$ to 7ka BP) are excluded owing to the potential for
247 artefacts; the depth range of the bubble-clathrate transition zone is based on observed positive anomalies in
248 $\delta\text{O}_2/\text{N}_2$ in WDC ice.

249 All samples were analyzed at Scripps Institution of Oceanography, USA, with the exception of the EDC
250 samples which were analyzed at University of Bern, Switzerland (Baggenstos et al., 2019). Some of the
251 EDC samples analyzed had clear evidence of drill liquid contamination, which acts to artefactually lower
252 $^{86}\text{Kr}_{\text{xs}}$ via isobaric interference on mass 82; the late Holocene data used here were not flagged for drill liquid
253 contamination (Baggenstos et al., 2019).

254 The 2σ analytical precision of the $\delta^{15}\text{N}$, $\delta^{40}\text{Ar}$, and $\delta^{86}\text{Kr}$ measurements is around 3, 5 and 26 per meg,
255 respectively, based on the reproducibility of La Jolla Air measurements. Via standard error propagation,
256 this results in a ~ 22 per meg ‰^{-1} (2σ) analytical uncertainty for both $^{86}\text{Kr}_{\text{xs}40}$ and $^{86}\text{Kr}_{\text{xs}15}$ at a site like WDC
257 where $\delta^{40}\text{Ar} \approx 1.2 \text{‰}$. We have no true (same-depth) replicates to assess the reproducibility of $^{86}\text{Kr}_{\text{xs}}$
258 measurements experimentally. The measured isotope ratios are corrected for gas loss (Δ_{GL}^{40}) and thermal
259 fractionation (Δ_{TF}^{86} , Δ_{TF}^{40} , Δ_{TF}^{15}) before interpretation; details on these corrections are given in appendix A.
260 For the coretop calibration study, the average magnitude of the gas loss and thermal fractionation
261 corrections is +14 and -15 per meg ‰^{-1} in $^{86}\text{Kr}_{\text{xs}}$, respectively. Note that these two corrections both involve
262 the $\delta^{40}\text{Ar}$ isotopic ratio, and therefore they are not independent from each other and not additive – in other
263 words, the total correction is not simply the sum of the two individual corrections.

264 Our study includes two ice cores from the Antarctic Peninsula: BRP (2 ice samples) and JRI (5 ice samples).
265 Measured $\delta\text{Xe}/\text{N}_2$ ratios (and to a lesser extent the $\delta\text{Kr}/\text{N}_2$ ratios) in all samples from both locations are
266 significantly elevated above the expected gravitational enrichment signal (Fig. A1A), which is clear
267 evidence for the presence of refrozen meltwater in these samples (Orsi et al., 2015). Like xenon, krypton is
268 highly soluble in (melt)water, and therefore $^{86}\text{Kr}_{\text{xs}}$ cannot be reliably measured in these samples; we reject
269 all samples from the BRP and JRI sites. It is notable that all samples from both sites show evidence of
270 refrozen meltwater, given that the high-accumulation BRP core is nearly entirely free of visible melt layers,
271 and that we carefully selected samples without visible melt features at JRI. Visible ice lenses form only
272 when meltwater pools and refreezes on top of low-permeability layers such as wind crusts; our observations
273 suggest meltwater can also refreeze throughout the firn in a way that cannot be detected visually.

274

275 3 Calibrating Kr-86 excess

276 The $^{86}\text{Kr}_{\text{xs}}$ proxy for synoptic activity was first proposed on theoretical grounds by Buizert and
277 Severinghaus (2016) – here we provide the first experimental validation of this proxy using a coretop
278 calibration of $^{86}\text{Kr}_{\text{xs}}$ using late-Holocene ice core samples from nine locations around Antarctica and one in
279 Greenland that represent a wide range of pressure variability in the modern climate (here: 1979-2017 CE).

280 3.1 Spatial variation in synoptic-scale pressure variability

281 Kr-86 excess is sensitive to air movement (both upward and downward), which in turn is controlled by the
282 magnitude of relative air pressure change. Let p_i be a time series of (synoptic-scale) site surface pressure
283 with N data points, time resolution Δt , and mean value \bar{p} . The time series can span a month, year, or multi-
284 year period, with \bar{p} potentially different for each month or year. We define the parameter Φ as:

$$285 \quad \Phi = \frac{1}{N\bar{p}} \sum_{i=1}^N \left| \frac{p_i - p_{i-1}}{\Delta t} \right| \quad (5)$$

286 which we here express in convenient units of $\% \text{ day}^{-1}$. Φ reflects the intensity of barometric pumping in the
287 firn column. Note that Δt should be larger than ~ 1 hour (the timescale for the entire firn column to
288 equilibrate with the surface pressure), and smaller than about a day (in order to adequately resolve synoptic-
289 scale pressure events). Here we use ERA-interim reanalysis data from 1979-2017 with $\Delta t = 6$ hours (Dee
290 et al., 2011), from which we calculate monthly and annual Φ values using Eq. (5). A map of annual-mean
291 Φ across Antarctica is given in Fig. 2A. At all sites considered, Φ has a strong seasonal cycle with pressure
292 variability/storminess being strongest in the local winter season (Fig. 2C). Interannual differences in Φ are
293 greatest along the Siple coast and coastal West Antarctica (Fig. 2B), mainly reflecting the influence of
294 central Pacific (ENSO, PDO) climate variability (Section 4).

295 3.2 Kr-86 excess proxy calibration

296 Present-day Antarctica has a wide range of Φ (Fig. 2A), which allows us to validate and calibrate $^{86}\text{Kr}_{\text{xs}}$. In
297 Fig. 3A we plot the site mean $^{86}\text{Kr}_{\text{xs}40}$ (with $\pm 1\sigma$ error bars) as a function of Φ (averaged over full 1979-
298 2017 period). We find a Pearson correlation coefficient of $r = -0.94$ when using site mean $^{86}\text{Kr}_{\text{xs}40}$, and $r =$
299 -0.83 when using the $^{86}\text{Kr}_{\text{xs}40}$ of individual samples, respectively ($p < 0.01$). Note that in this particular case
300 the site-mean $^{86}\text{Kr}_{\text{xs}40}$ and $^{86}\text{Kr}_{\text{xs}15}$ are identical (because by design, after thermal correction $\delta^{15}\text{N} = \delta^{40}\text{Ar}$);
301 the error bars are different, though.

302 The $^{86}\text{Kr}_{\text{xs}}$ data have been corrected for gas loss (Appendix A1) and thermal fractionation (Appendix A2);
303 with the gas loss correction being the more uncertain component. Figure 3B shows the correlations of the
304 calibration curve as a function of the gas loss scaling parameter ϵ_{40} . We find a good correlation over a wide
305 range of ϵ_{40} values, proving our calibration is not dependent on the choice of ϵ_{40} . When using uncorrected
306 $^{86}\text{Kr}_{\text{xs}40}$ data the site mean correlation is $r = -0.71$; when applied individually, both the gas loss and thermal
307 correction each improve the correlation to $r = -0.77$ and $r = -0.79$, respectively (Fig. A3, all $p < 0.05$). Based
308 on these tests we conclude that the observed relationship is not an artefact of the applied corrections. The
309 applied corrections improve the correlation, which increases confidence in the method. The calibration
310 results for $^{86}\text{Kr}_{\text{xs}15}$ are shown in Fig. A4.

311 Notably, there is a large spread in $^{86}\text{Kr}_{\text{xs}}$ across samples from any single site, particularly at the high- Φ sites
312 of SDM and RICE (Fig. 3A, note the $\pm 1\sigma$ error bars). This spread is larger than the measurement
313 uncertainty, and we believe this variance reflects a signal that is truly present in the ice. The Siple coast and
314 Roosevelt Island experience the largest Φ interannual differences in Antarctica (Fig. 2B), and it is therefore
315 likely that our coarse sampling is aliasing the true $^{86}\text{Kr}_{\text{xs}}$ signal. The variance in $^{86}\text{Kr}_{\text{xs}}$ may contain climate
316 information also.

317 Both theoretical considerations and observations thus suggest $^{86}\text{Kr}_{\text{xs}}$ is a proxy for time-averaged barometric
318 surface pressure variability at the site, and in the remainder of this manuscript we will interpret it as such.

319 **3.3 Discussion of the Kr-86 excess proxy**

320 Our interpretation of $^{86}\text{Kr}_{\text{xs}}$ as a proxy for time-averaged pressure variability is somewhat complicated by
321 the possibility of deep convective zones, which have the same $^{86}\text{Kr}_{\text{xs}}$ signature as barometric pumping. This
322 was discovered at the Megadunes (MD) site, central East Antarctica; at this zero-accumulation site deep
323 cracks form in the firn layer that facilitate a 23 m deep convection zone (Severinghaus et al., 2010). In fact,
324 this observation led earlier work to suggest that noble gas gravitational disequilibrium may be used as a
325 proxy for convective zone thickness (Kawamura et al., 2013), rather than synoptic-scale pressure variability
326 as suggested here. Although megadunes and zero-accumulation zones are ubiquitous and cover 20% of the
327 Antarctic Plateau (Fahnestock et al., 2000), ice cores are seldom drilled in these areas and it is safe to
328 assume that they never formed at sites like WAIS Divide that had relatively high accumulation rates even
329 during the last glacial period. Performing the corrections for thermal and size-dependent fractionation is
330 challenging at MD, and we suggest that the MD $^{86}\text{Kr}_{\text{xs}}$ is in the range of -2 to -55 per meg ‰^{-1} ; even at the
331 larger limit, this is still smaller in magnitude than $^{86}\text{Kr}_{\text{xs}}$ anomalies at several modern-day sites with small
332 convective zones (such as SDM, RICE and the Law Dome sites), suggesting barometric pumping is capable
333 of producing larger $^{86}\text{Kr}_{\text{xs}}$ signals than even the most extreme observed case of convective surface mixing.
334 Having $^{86}\text{Kr}_{\text{xs}}$ measured in MD ice core (rather than firn air) samples would be valuable for a more
335 meaningful comparison to the ice core sample measurements presented here. Windy sites can have
336 substantial convective zones of ~ 14 m (Kawamura et al., 2006), and future studies of $^{86}\text{Kr}_{\text{xs}}$ at such sites
337 would be valuable.

338 Currently, 1-D and 2-D firn air transport model simulations underestimate the magnitude of the $^{86}\text{Kr}_{\text{xs}}$ signal
339 compared to measurements in mature ice samples (Birner et al., 2018), complicating scientific
340 understanding of the proxy. In these models, the effective molecular diffusivity of each gas is scaled linearly
341 to its free air diffusivity. The ratio of krypton to argon free air diffusivity is 0.78. This ratio, which directly
342 sets the magnitude of the simulated $^{86}\text{Kr}_{\text{xs}}$, may actually be smaller than 0.78 in real firn, as krypton is more
343 readily adsorbed onto firn surfaces retarding its movement (similar to gasses moving through a gas
344 chromatography column). This may be one explanation for why models simulate too little $^{86}\text{Kr}_{\text{xs}}$.

345 Another likely explanation for the model-data mismatch is that certain critical sub-grid processes (such as
346 the aforementioned pore-size dependence of the Péclet number) are not adequately represented in these
347 models. Barometric pumping may further actively shape the pore network through the movement of water
348 vapor, thereby keeping certain preferred pathways connected and open below the density where percolation
349 theory would predict their closure (Schaller et al., 2017). The fate of a pore restriction is determined by the
350 balance between the hydrostatic pressure (that acts to close it) and vapor movement away from its convex

351 surfaces (that acts to keep it open); we speculate that barometric Darcy air flow keeps high-flow channels
352 connected longer by eroding convex surfaces. This enhances the complexity (and therefore dispersivity) of
353 the deep firn pore network and possibly creates a non-linear $^{86}\text{Kr}_{\text{xs}}$ response to barometric pumping. The
354 hypothesized channel formation in deep firn is driven by a positive feedback on flow volume, and somewhat
355 reminiscent of erosion-driven stream network formation in fluvial geomorphology.

356 Firn models predict that, after correcting for thermal fractionation, the deviation from gravitational
357 equilibrium for the elemental ratios (such as $\delta\text{Kr}/\text{Ar}$) should be proportional to that deviation in isotopic
358 ratios. However, the observations suggest that the former is usually smaller than would be expected from
359 the latter. As before, adsorption of Kr onto firn grain surfaces may contribute to the observed discrepancy,
360 and laboratory tests of this process are called for. Further, the impacts of gas loss are greater on elemental
361 ratios than on the isotopic ratios which may contribute also. Including measurements of xenon isotopes and
362 elemental ratios in future measurement campaigns may be able to provide additional constraints to better
363 understand this discrepancy.

364 Measurements on firn air samples, where available, suggest a smaller $^{86}\text{Kr}_{\text{xs}}$ anomaly in firn air than found
365 in ice core samples from the same site. We attribute this in part to a seasonal bias that is introduced by the
366 fact that firn air sampling always takes place during the summer months, whereas the synoptic variability
367 that drives the Kr-86 excess anomalies is largest during the winter (Fig. 2C); consequently, firn air
368 observations are biased towards weaker $^{86}\text{Kr}_{\text{xs}}$. Further, in the deep firn where $^{86}\text{Kr}_{\text{xs}}$ anomalies are largest,
369 firn air pumping may not yield a representative air sample, but rather be biased towards the well-connected
370 porosity at the expense of poorly-connected cul-de-sac-like pore clusters. Since barometric pumping
371 ventilates this well-connected porespace with low- $^{86}\text{Kr}_{\text{xs}}$ air from shallower depths, the firn air sampling
372 may not capture a representative $^{86}\text{Kr}_{\text{xs}}$ value of the full firn air content. These explanations are all somewhat
373 speculative, and a definitive understanding of the firn-ice differences is lacking at this stage.

374 Gas loss and thermal corrections are critical to the interpretation of $^{86}\text{Kr}_{\text{xs}}$. The thermal correction is applied
375 to account for thermal gradients in the firn (ΔT , here defined as the temperature at the top minus the
376 temperature at the base of the firn), which are chiefly caused by geothermal heat or surface temperature
377 changes at the site. At low-accumulation sites geothermal heating leads to $\Delta T < 0$. We use ^{15}N -excess ($\delta^{15}\text{N}$
378 $- \delta^{40}\text{Ar}/4$) to estimate the thermal gradient in the firn (Appendix A2). Because nitrogen and argon have
379 similar diffusivities but different thermal diffusion coefficients, $\delta^{15}\text{N} - \delta^{40}\text{Ar}$ is relatively insensitive to
380 barometric pumping yet sensitive to thermal fractionation, allowing estimating ΔT .

381 Besides the actual thermal gradients in the firn, the isotopic composition may also be impacted by seasonal
382 rectifier effects. If the firn air transport properties differ between the seasons (for example due to thermal
383 contraction cracks, convective instabilities, or seasonality in wind pumping), this can result in a thermal
384 fractionation of isotopic ratios in the absence of a thermal gradient (Morgan et al., 2022).

385 For the WDC, DSS and GISP2 sites we obtain ΔT values close to zero as expected for these high-
386 accumulation sites; for the SP, SDM, RICE, and DF sites we find ΔT ranging from -0.76 to -1.18°C, in
387 agreement with the effect of geothermal heat. The high-accumulation DE08 and DE08-OH sites both have
388 an unexpectedly large ΔT of -1.6°C; the good agreement between the sites suggest it is likely a real signal,
389 yet we can rule out geothermal heat as the cause. This may suggest that the Law Dome DE08 site is subject

390 to a seasonal rectifier effect, or a recent climatic cooling. Last, the EDC site shows an unexpected $\Delta T =$
391 $+1.6 \pm 1.89^\circ\text{C}$. Three possible explanations are: (1) the aforementioned drill liquid contamination for this
392 core (Baggenstos et al., 2019); (2) a summertime-biased seasonal rectifier; or (3) an over-correction of
393 $\delta^{40}\text{Ar}$ for gas loss, which could occur for example if natural and post-coring fugitive gas loss fractionate
394 $\delta^{40}\text{Ar}$ differently and EDC samples were impacted mostly by the former type (our correction is mostly
395 based on measurements of the latter type).

396 For the Law Dome DE08-OH site we observe large (5-fold) sub-annual variations in $^{86}\text{Kr}_{\text{xs}}$ (Fig. B1). The
397 magnitude of the $^{86}\text{Kr}_{\text{xs}}$ layering is truly remarkable. The isotopic enrichment of each gas ($\delta^{15}\text{N}$, $\delta^{40}\text{Ar}$,
398 $\delta^{86}\text{Kr}$) can be converted to an effective diffusive column height (DCH). For the samples with the smallest
399 (greatest) $^{86}\text{Kr}_{\text{xs}}$ magnitude, this DCH is around 1 m (6 m) shorter for $\delta^{86}\text{Kr}$ than it is for $\delta^{15}\text{N}$. The firn air
400 transport physics that may explain such phenomena are beyond our current scientific understanding. The
401 sub-annual variations may be related to the seasonal cycle in storminess, though that seems improbable to
402 us at present as the gas age distribution at the depth of bubble closure has a width of several years
403 (Schwander et al., 1993). Another reason may be seasonal layering in firn properties – such as density,
404 grain size, and pore connectivity – that control the degree of disorder and dispersive mixing occurring in
405 the firn, and lead to a staggered firn trapping and seasonal variations in ΔAge (Etheridge et al., 1992; Rhodes
406 et al., 2016). The sample air content estimated from the IRMS inlet pressure is similar for all measurements,
407 making it unlikely that the variations in $^{86}\text{Kr}_{\text{xs}}$ are caused by remnant open porosity in lower-density layers.
408 In any case it is remarkable that such large variations in gas composition can arise and persist on such small
409 length scales, given the relatively large diffusive, dispersive, and advective transport length scales of the
410 system. More work is needed to establish the origin of the sub-annual variations in ice core $^{86}\text{Kr}_{\text{xs}}$. At all
411 other sites analyzed here, the sample length exceeds the annual layer thickness; this will remove some, but
412 not all, of the effects of the sub-annual variations.

413 Another puzzling observation is the positive $^{86}\text{Kr}_{\text{xs}}$ at the Dome Fuji (DF) site; theoretical considerations
414 suggest it should always be negative. In part this may be due to an over-correction of $\delta^{40}\text{Ar}$ for gas loss,
415 which would act to bias $^{86}\text{Kr}_{\text{xs}}$ in the positive direction. This correction is largest at DF owing to the very
416 negative $\delta\text{O}_2/\text{N}_2$ and $\delta\text{Ar}/\text{N}_2$ (Fig. A1); while we base our correction on published work, it is conceivable
417 that we overestimate the true correction (Appendix A1). In particular, our gas loss correction is based on
418 observations on artefactual post-coring gas loss, which may fractionate $\delta^{40}\text{Ar}$ differently than natural
419 fugitive gas loss during bubble close-off. Omitting the gas loss correction indeed makes $^{86}\text{Kr}_{\text{xs}}$ at DF
420 negative (Fig. A3C-D). Another hypothesis is that the positive $^{86}\text{Kr}_{\text{xs}}$ signal is an artefact of the seasonal
421 rectifier that Morgan et al. (2022) identify at DF. In this work we assume a linear approach in which the
422 effect of the rectifier can be described by a single ΔT value that is the same for isotopic pairs. In reality,
423 there may be non-linear interactions between thermal fractionation and firn advection that impact the
424 isotopic values of the various gases in a more complex way than captured in our approach.

425 The $^{86}\text{Kr}_{\text{xs}}$ is also correlated with other site characteristics besides Φ . For site elevation we find $r = 0.96$
426 (0.84); and for mean annual temperature $r = -0.87$ (-0.76); the number in parentheses gives the correlation
427 when using all the individual samples rather than site-mean $^{86}\text{Kr}_{\text{xs}}$. The listed correlations all have $p < 0.01$.
428 For site accumulation we do not find a statistically significant correlation at the 90% confidence level. The
429 correlations with elevation and temperature are comparable to those we find for Φ ; this is no surprise given
430 that elevation, Φ and T are all strongly correlated with one another, mainly because elevation directly

431 impacts both T (via the lapse rate) and Φ (via its topographic influence on the position of storm tracks). To
432 our knowledge there are no mechanisms through which either elevation or annual-mean temperature could
433 drive kinetic isotopic fractionation in the firn layer. Perhaps other unexamined site characteristics (such as
434 the degree of density layering, or the magnitude of the annual temperature cycle) could provide good
435 correlations also, suggesting additional hidden controls on $^{86}\text{Kr}_{\text{xs}}$. The data needed to assess such hidden
436 controls are not available for most sites.

437 The calibration of the $^{86}\text{Kr}_{\text{xs}}$ proxy is based on spatial regression. In applying the proxy relationship to
438 temporal records, we make the implicit assumption that proxy behavior in the temporal and spatial
439 dimensions is at least qualitatively similar. This assumption may prove incorrect. In particular, changes in
440 insolation are known to impact firn microstructure and bubble close-off characteristics, which in turn
441 impacts gas records of $\delta\text{O}_2/\text{N}_2$ and total air content (Bender, 2002; Raynaud et al., 2007). Since $^{86}\text{Kr}_{\text{xs}}$ is
442 linked to the dispersivity of deep firn, it seems probable that insolation has a direct impact on $^{86}\text{Kr}_{\text{xs}}$ also via
443 the firn microstructure. We will revisit this issue in our interpretation of the WDC $^{86}\text{Kr}_{\text{xs}}$ record (Section 5).
444 Overall, we anticipate $^{86}\text{Kr}_{\text{xs}}$ to be a qualitative proxy for synoptic variability, yet want to caution against
445 quantitative interpretation based on the spatial regression slope.

446 The observations presented in this section clearly highlight the fundamental shortcomings of our current
447 understanding of firn air transport hinting at the existence of complex interactions, presumably at the pore-
448 scale, that are not being represented. Percolation theory finds that near the critical point (presumably the
449 lock-in depth) a network becomes fractal in its nature; we suggest that this fractal nature of the pore network
450 likely contributes to non-linear pore-scale interactions that give rise to the $^{86}\text{Kr}_{\text{xs}}$ observations in ice. While
451 the observed correlation of Fig. 3A is highly encouraging, further work is critical to understand this proxy.
452 Examples of such future studies are: (1) additional high-resolution records that can resolve the true
453 variations that exist in a single ice core, similar to the DE08-OH record; (2) 3-D firn air transport model
454 studies; (3) improvements to the gas loss correction; (4) additional coring sites to extend the spatial
455 calibration and further confirm the validity of the proxy; (5) Adding xenon isotopic constraints (^{136}Xe
456 excess) as an additional marker of isotopic disequilibrium; (6) numerical simulations of pore-scale air
457 transport in large-scale firn networks; (7) experimental studies of dispersion and noble gas adsorption in
458 firn samples; (8) percolation theory approaches to study the fractal nature of the pore network of the lock-
459 in zone; and (9) replication of the WDC deglacial $^{86}\text{Kr}_{\text{xs}}$ record in nearby ice cores such as RICE.

460 **4 Present-day controls on Kr-86 excess in Antarctica**

461 In this section we investigate the large-scale patterns of climate variability in the Southern Hemisphere that
462 could affect Φ and therefore $^{86}\text{Kr}_{\text{xs}}$ over Antarctica. We begin by investigating the patterns in the wind field
463 that are associated with changes in Φ at ice core sites, before examining how more canonical patterns of
464 Southern Hemisphere climate variability, such as the southern annular mode (SAM), might affect Φ over
465 the whole of Antarctica.

466 We use ERA-interim reanalysis data for the 1979-2017 period (Dee et al., 2011) to evaluate the present-
467 day controls on synoptic-scale pressure variability in Antarctica. Kr-86 excess in an ice core sample
468 averages over several years of pressure variability, and therefore we focus on annual-mean correlation in
469 our analysis. The annual-mean Φ is calculated from the 6-hourly reanalysis data using Eq. (5). Note that
470 we let the year run from April to March to avoid dividing single El Niño / La Niña events across multiple
471 years.

472 At all Antarctic sites investigated, a similar pattern exists; four representative locations are shown in Fig.
473 4, where we regress the zonal wind in the lower (850 hPa, color shading) and upper troposphere (200 hPa,
474 contours) onto our surface pressure variability parameter Φ . We find that synoptic pressure variability at
475 these sites is linked to zonal winds along the southern margin of the eddy-driven subpolar jet (SPJ), which
476 extends from the surface to the upper troposphere (Nakamura and Shimpo, 2004; Trenberth, 1991). Sites
477 near the ice sheet margin (Figs. 4A, B and D) are most sensitive to the SPJ edge in their sector of Antarctica,
478 whereas interior sites (Fig. 4C) appear sensitive to the overall strength/position of the SPJ. Note that
479 strengthening, broadening or southward shifting of the SPJ all can in principle enhance site Φ .

480 Pressure variability at WDC is furthermore correlated with the strength of the Pacific Subtropical jet (STJ)
481 aloft (solid contour lines centered around 30°S in the Pacific in panel 4A), forming an upper troposphere
482 wind pattern that resembles the wintertime South Pacific split jet (Bals-Elsholz et al., 2001; Nakamura and
483 Shimpo, 2004); this agrees with the finding that a strengthening of the split jet enhances storminess over
484 West Antarctica (Chiang et al., 2014).

485 Next, we investigate how the well-known patterns of large-scale atmospheric variability, such as SAM and
486 ENSO, impact pressure variability in Antarctica. Figure 5 shows the correlation of Φ with the three leading
487 modes of SH extra-tropical atmospheric variability; the correlation with various indices and modes for
488 individual ice core locations is given in Table 2. Most teleconnection patterns have a specific season during
489 which they are strongest; here we do not differentiate between seasons, because $^{86}\text{Kr}_{\text{xs}}$ in ice core samples
490 averages over all seasons.

491 Globally, annual-mean Φ is highest over the Southern Ocean (Fig. 5A); a region of enhanced baroclinicity
492 associated with the eddy-driven SPJ (Nakamura and Shimpo, 2004). The green line denotes the latitude of
493 maximum Φ , corresponding roughly to the latitude with the highest storm track density (57.8°S on average).

494 The dominant mode of atmospheric variability in the SH extratropics is the southern annular mode,
495 representing the vacillation of atmospheric mass between the mid- and high-latitudes (Thompson and
496 Wallace, 2000). Figure 5B shows 500 hPa geopotential height (Z500) anomalies associated with the SAM
497 as contours, with the color shading giving the correlation between Φ and the SAM index. During the

498 positive SAM phase (negative Z500 over Antarctica) we find that the stormtracks and maximum synoptic
499 activity are displaced towards Antarctica (positive Φ correlation poleward of the green line in Fig. 5B).
500 This is associated with a strengthening and poleward displacement of the SH westerly winds that occurs
501 during a positive SAM phase. More locally, Φ on the Antarctic Peninsula is positively correlated with the
502 SAM-index (Table 2); Φ at the other sites is not meaningfully impacted. This suggests that the variations
503 associated with the SAM (as commonly defined) do not extend far enough poleward to meaningfully impact
504 Antarctica with the exception of the Peninsula. Enhanced synoptic variability on the Peninsula during
505 positive SAM phases is consistent with observations of enhanced snowfall at those times (Thomas et al.,
506 2008).

507 The second mode of SH extratropical variability is the Pacific-South American Mode 1 (PSA1), which
508 reflects a Rossby wave response to sea surface temperature (SST) anomalies over the central and eastern
509 equatorial Pacific (Mo and Paegle, 2001), and is therefore closely linked to ENSO on interannual time
510 scales (we find a correlation of $r = 0.77$ between the annual mean PSA1 and Niño 3.4 indices). Φ in the
511 Amundsen and Ross Sea sectors (WDC, SDM and RICE) is positively correlated to the PSA1 and Niño 3.4
512 SST, suggesting larger synoptic activity during El Niño phases and low activity during La Niña phases. The
513 PSA2 pattern, also linked to SST anomalies in the tropical Pacific (Mo and Paegle, 2001), is likewise
514 correlated to Φ in the Amundsen and Ross Sea sectors (Fig. 5C and Table 2). While all the correlations
515 listed are statistically significant, they explain only a fraction of the total variability.

516 Next, we consider anomalies in sea ice area and extent (Parkinson and Cavalieri, 2012). We focus on the
517 Ross and Amundsen-Bellingshausen Seas where impacts on WAIS Divide may be expected. At the 90%
518 confidence level we do not find significant correlations to sea ice area or extent at most core locations
519 (Table 2). Correlations to sea ice extent are (even) weaker than those for sea ice area and consequently not
520 shown. We performed a lead-lag study of the correlations between Φ and sea ice area/extent in the various
521 sectors, and find that in all cases maximum correlations occur for the sea ice changes lagging 0 to 4 months
522 behind Φ ; we interpret this to mean that the sea ice is responding to changes in atmospheric circulation,
523 rather than driving them.

524 Overall, we find that synoptic activity at WAIS Divide, the site of most interest here, is controlled by the
525 position and/or strength of the stormtracks at the southern edge of the SPJ in the Pacific sector of the
526 Southern Ocean (Ross, Amundsen and Bellingshausen Seas), with little sensitivity to the SPJ behavior in
527 the other sectors. Owing to its remote southern location, WDC is only weakly impacted by the commonly-
528 defined large-scale modes of atmospheric variability. Most notably, WDC has a modest influence from the
529 tropical Pacific climate, as shown by a correlation around $r \approx 0.3$ to the PSA1, Niño 3.4 and PDO indices
530 (Table 2). We further find statistically significant correlations (up to $r = 0.44$) between WDC Φ and SST
531 in broad regions of the central and eastern tropical Pacific (not shown). We suggest that ENSO weakly
532 impacts storminess at WDC (around 10% of variance explained) via its impact on the SPJ in the South
533 Pacific.

534 **5 Barometric variability in West Antarctica during the last deglaciation**

535 **5.1 The 0-24 ka WAIS Divide Kr-86 excess record**

536 The WAIS Divide downcore $^{86}\text{Kr}_{\text{xs}}$ dataset we present here was produced during five separate measurement
537 campaigns that occurred in February-April 2014, February-April 2015, August 2015, August 2020, and
538 August 2021, respectively. Campaigns 1-3 were reported previously (Bereiter et al., 2018a; Bereiter et al.,
539 2018b), and campaigns 4 and 5 were meant to resolve conflicts between the $^{86}\text{Kr}_{\text{xs}}$ data sets from these
540 earlier campaigns. Three slightly different measurement approaches were used. Campaign 1 uses “Method
541 1” from Bereiter et al. (2018a), in which the air sample splitting is done in a water bath for over 12 hours
542 to equilibrate the sample. Campaigns 2 and 3 use “Method 2” from Bereiter et al. (2018a), in which a
543 bellows is used to split the air samples for over 4 to 6 hours. Campaigns 4 and 5 do not involve splitting of
544 the air sample, and only analyzed the Kr and Ar isotopic ratios. During campaign 4 a glass bead from the
545 water trap had gotten stuck in the tubing, restricting the flow and likely resulting in incomplete air extraction
546 from the melt water.

547 Figure 6 compares $^{86}\text{Kr}_{\text{xs}40}$ (panel A) and $^{86}\text{Kr}_{\text{xs}15}$ (panel B) from the five campaigns. Campaign 1 is the
548 only campaign that spans the full age range of the record, making it the most valuable of the three
549 campaigns. Campaigns 2 and 3 are mostly restricted to the Pleistocene and Holocene periods respectively,
550 with little overlap between them. Campaigns 4 and 5 aimed to reproduce some of the most salient features
551 in the earlier three.

552 No true replicate samples were analyzed between the campaigns, in part because the large sample size
553 requirement precludes this. To assess offsets, we rely on nearest-neighbor linear interpolation. We find an
554 offset of 5 per meg between the first and second campaign (during their period of overlap); this is within
555 the analytical precision (22 per meg), suggesting these two campaigns are in good agreement. The
556 agreement is good for both the $^{86}\text{Kr}_{\text{xs}40}$ and $^{86}\text{Kr}_{\text{xs}15}$ definitions. The first downcore campaign furthermore
557 overlaps in depth with the WDC calibration dataset (gray data in Fig. 6); we find no offset between those
558 data sets either. Data from campaign 2 appear to have more scatter, possibly reflecting the shorter
559 equilibration time during sample splitting.

560 We combine data from the first two campaigns, and evaluate their offset to data from the other three
561 campaigns using nearest-neighbor linear interpolation. For campaigns 3, 4 and 5 we find an offset of -31,
562 -22 and -23 per meg $\%^{-1}$ in $^{86}\text{Kr}_{\text{xs}40}$, respectively. For campaign 3 the offset is -34 per meg $\%^{-1}$ in $^{86}\text{Kr}_{\text{xs}15}$.
563 It is remarkable that all three later campaigns are more negative in $^{86}\text{Kr}_{\text{xs}}$ than the first two. Campaign 3
564 shows the greatest offset (greater than analytical precision), and has more scatter in both $^{86}\text{Kr}_{\text{xs}}$ (Fig. 6) and
565 ^{15}N excess (Fig. A5), and less care was taken during this campaign that the IRMS conditions were stable.
566 The offset of campaign 4 may be attributed to the incomplete sample transfer due to the bead stuck in the
567 line. The offset in campaign 5 is hard to explain. The systematically more negative $^{86}\text{Kr}_{\text{xs}}$ of campaigns 4
568 and 5 may reflect sample storage effects, as these were measured 5-6 years after campaign 1 and 2. However
569 this would not explain the negative values of campaign 3. The good $^{86}\text{Kr}_{\text{xs}}$ agreement between DE08 and
570 DE08-OH, drilled 32 years apart, would also argue against large storage effects. For campaign 4 and 5 only
571 Ar and Kr isotope ratios were measured, and so we lack typical tracers of gas loss ($\delta\text{O}_2/\text{N}_2$ and $\delta\text{Ar}/\text{N}_2$.)

572 In the remainder of this paper we will interpret the combined data from campaigns 1 and 2, but with the
573 caveat that there is a persistent offset with later campaigns. However, the features we interpret are
574 corroborated by the later campaigns, if one takes the offset into account. To aid interpretation of the data,
575 we apply a Gaussian smoothing spline with a smoothing filter width that varies depending on the data
576 density (from 250-year width in the deglaciation itself where the data density is high, to 1750 years in the
577 Holocene and LGM where data density is low). To estimate the uncertainty in the smoothing spline we use
578 a Monte Carlo approach that considers uncertainty in (1) the gas loss correction, by randomly sampling ϵ_{40}
579 in the range of 0 to -0.008; (2) the thermal correction, by randomly scaling the thermal scenario (Fig. A5)
580 by a factor ranging from 0 to 2; and (3) analytical errors, by adding random errors to individual data points
581 drawn from a normal distribution with a 2σ width of 22 per meg. The $\pm 1\sigma$ uncertainty range with mean
582 value are shown as the gray envelope and center line in Fig. 6. We believe the following observations to be
583 robust:

- 584 • The Holocene shows a trend towards increasingly negative $^{86}\text{Kr}_{\text{xs}}$, suggesting a gradual increase in
585 synoptic activity toward the present. Minimum synoptic activity in West Antarctica occurs during the
586 early Holocene around 10 ka BP; the Monte Carlo study suggests $^{86}\text{Kr}_{\text{xs}40}$ in the early Holocene (8ka-
587 10ka BP) is 30.5 ± 18 per meg ‰^{-1} ($\pm 2\sigma$) below the late-Holocene value (last 2 ka). Using the slope of
588 our core-top calibration (Fig. 3), we estimate that early-Holocene WDC synoptic activity Φ is $\sim 17\%$
589 weaker than it is today. This change is comparable to the 2σ magnitude of interannual variations in
590 annual mean Φ at the site today (or about half the peak-to-peak variations thereof). This Holocene trend
591 is seen in the data from campaigns 1, 3 and 4. Campaign 5 does not suggest a trend but has only one
592 late Holocene data point making it less robust. The trend in campaign 3 is less robust due to the greater
593 scatter in the data.
- 594 • The most pronounced change occurs at the Younger Dryas (YD) - Holocene transition, where $^{86}\text{Kr}_{\text{xs}}$
595 becomes more positive (by 30.1 ± 16 per meg ‰^{-1} , comparing YD and early Holocene) implying a
596 decrease in synoptic activity. This transition is observed in campaigns 1, 2, 4 and 5 that cover this time
597 period (the third campaign does not cover it), and represents a $\sim 17\%$ drop in synoptic activity (Φ).
- 598 • During the Last Glacial Maximum (LGM), WDC synoptic activity was perhaps slightly weaker than at
599 present, but not significantly so ($^{86}\text{Kr}_{\text{xs}40}$ more positive by 11 ± 13 per meg ‰^{-1}). The West Antarctic
600 ice sheet elevation was likely higher during the LGM, and a 300 m elevation increase would by itself
601 increase $^{86}\text{Kr}_{\text{xs}40}$ by 10 per meg ‰^{-1} , all else being equal (Appendix A3); this is within the analytical
602 error of our observations. This feature is seen in campaign 1 and not covered by the other campaigns.
- 603 • The deglaciation itself has enhanced synoptic activity, in particular during the two North-Atlantic cold
604 stages Heinrich Stadial 1 (HS1) and the YD as highlighted with yellow bars in Figs. 6 and 7. Synoptic
605 activity during these periods is enhanced relative to the adjacent LGM and early Holocene, yet
606 comparable to today. This feature is seen in campaigns 1 and 2, and in 4 and 5 for the transition into
607 the Holocene.

608 Below we will interpret the deglacial WDC $^{86}\text{Kr}_{\text{xs}}$ record in terms of time-averaged barometric variability.
609 Before doing so we want to emphasize that firn processes may have been imprinted onto the record also, in
610 particular on orbital timescales where firn microstructure responds to local (summer) insolation intensity
611 (Bender, 2002). High summer insolation results in more depleted $\delta\text{O}_2/\text{N}_2$ and reduced air content, likely via
612 stronger layering and a delayed pore close-off process (Fujita et al., 2009).

613 Local summer solstice insolation in Antarctica increases through the Holocene, with the highest values in
614 the late Holocene. This may impact $^{86}\text{Kr}_{\text{xs}}$, although it is not a-priori clear what the sign of this relationship
615 would be. The sense of the Holocene temporal trends is that a more negative $^{86}\text{Kr}_{\text{xs}}$ coincides with more
616 negative $\delta\text{O}_2/\text{N}_2$. Note that this is opposite to the trends seen in the spatial calibration, where sites with the
617 most negative $\delta\text{O}_2/\text{N}_2$ (DF, SP, EDC) have the most positive $^{86}\text{Kr}_{\text{xs}}$. For now, the impact of local insolation
618 on $^{86}\text{Kr}_{\text{xs}}$ via firn microstructure remains unknown, which is an important caveat in interpreting the orbital-
619 scale changes in WDC $^{86}\text{Kr}_{\text{xs}}$. The abrupt $^{86}\text{Kr}_{\text{xs}}$ increase at the Holocene onset is too abrupt to be caused by
620 insolation changes, and thus we can interpret that change with more confidence.

621 The scatter in the late Holocene WDC $^{86}\text{Kr}_{\text{xs}}$ data exceeds the stated analytical precision. Potential
622 explanations include (1) an underestimation of the true analytical precision; (2) interannual to decadal
623 variations in storminess at WDC; and (3) aliasing of cm-scale variations in ice core $^{86}\text{Kr}_{\text{xs}}$ linked to layering
624 in firn microstructural properties.

625 **5.2 Barometric variability at WAIS Divide during the last deglaciation**

626 In the present-day, synoptic-scale pressure variability at WAIS Divide is correlated with zonal wind
627 strength along the southern margin of the SPJ (Section 4). In our interpretation, a more negative $^{86}\text{Kr}_{\text{xs}}$
628 reflects a strengthening or southward shift of the SPJ in the Pacific sector. Here we provide a climatic
629 interpretation of the deglacial WDC $^{86}\text{Kr}_{\text{xs}}$ record, and suggest that variations in synoptic variability at WDC
630 are linked to meridional movement of the ITCZ on millennial and orbital timescales.

631 The main features of the deglacial WDC $^{86}\text{Kr}_{\text{xs}}$ record listed in Section 5.1 resemble similar features seen
632 in records of (sub-) tropical hydrology and monsoon strength, such as the speleothem calcite $\delta^{18}\text{O}$ records
633 from Hulu Cave, China (Fig. 7C) and from Botuvera cave, southern Brazil (Fig. 7D), which are thought to
634 reflect the intensity of the East Asian and South American summer monsoons, respectively (Cruz et al.,
635 2005; Wang et al., 2007; Wang et al., 2001). These two monsoon records are anti-correlated, showing
636 opposing rainfall trends between the NH and SH on both orbital and millennial timescales. This pattern is
637 commonly attributed to displacement of the mean meridional position of the ITCZ (Chiang and Friedman,
638 2012; McGee et al., 2014; Schneider et al., 2014), driven by hemispheric temperature differences (Fig. 7B).
639 On orbital timescales such ITCZ migration has a strong precessional component, moving towards the
640 hemisphere with more intense summer peak insolation; on millennial timescales the ITCZ responds to
641 abrupt North-Atlantic climate change associated with the D-O and Heinrich cycles (Broccoli et al., 2006;
642 Chiang and Bitz, 2005; Wang et al., 2001), which are in turn linked to changes in meridional heat transport
643 by the Atlantic meridional overturning circulation, or AMOC (Lynch-Stieglitz, 2017; Rahmstorf, 2002).

644 Changes in mean ITCZ position have a strong influence on the structure and strength of the SH jets. During
645 periods when the NH is relatively cold (such as D-O stadials or periods with negative orbital precession
646 index) the ITCZ is displaced southward and the SH Hadley cell is weakened, thereby also weakening the
647 SH upper-tropospheric subtropical jet (Ceppi et al., 2013; Chiang et al., 2014). The reverse is also true, with
648 the ITCZ shifted northward during NH warmth, associated with a strengthening of the SH Hadley cell and
649 STJ. In a range of model simulations (Ceppi et al., 2013; Lee and Kim, 2003; Lee et al., 2011; Pedro et al.,
650 2018) the weakening of the SH STJ (as during NH cold) is furthermore accompanied by a strengthening
651 and/or southward shift of the SPJ/eddy-driven jet and SH westerly winds. Recently, ice core observations
652 have confirmed in-phase shifts in the position of the SHW occur during the D-O cycle in parallel to those

653 of the ITCZ (Buizert et al., 2018; Markle et al., 2017). Marine records of fluvial sediment runoff off the
654 Chilean coast suggest precession-phased movement of the South Pacific SPJ, again in parallel to the ITCZ
655 movement (Lamy et al., 2019).

656 The SAM index reflects the meridional position of the SHW and eddy-driven jet. During positive SAM
657 phases the SHW are displaced poleward, and during negative phases equatorward. Present-day month-to-
658 month changes in SAM index represent a mode of internal variability, with anomalies persisting for only
659 weeks to months – the timescale is longest in late spring and early summer reflecting a stronger planetary
660 wave–mean flow interaction (Simpson et al., 2011; Thompson and Wallace, 2000). By contrast, shifts in
661 the ITCZ and SH jet structure on millennial and orbital timescales have a much longer lifetime and different
662 dynamics, being driven from the tropics via hemispherically asymmetric changes in Hadley cell and STJ
663 strength. Therefore, present-day SAM internal variability is not expected to be a good analogue for past
664 changes in SHW position. We find that the present-day SAM month-to-month internal variability mainly
665 impacts synoptic variability over the Southern Ocean and does not have a statistically significant WDC
666 (Table 2). Such variability is likely to have occurred during other climatic regimes also, possibly just
667 centered around a mean SHW position that is displaced meridionally relative to today. At first glance it
668 may appear contradictory to state, as we do, that synoptic activity at WDC is not sensitive to the SAM while
669 also suggesting that during the last deglaciation synoptic activity at WDC is linked to changes in the position
670 of the SH eddy-driven jet and westerlies. Based on the considerations above, both claims may be true
671 without contradiction.

672 Besides secular changes to the SPJ position/strength linked to meridional ITCZ movement, WDC $^{86}\text{Kr}_{\text{xs}}$
673 may also have imprints from ENSO and tropical Pacific climate. Our analysis suggests a weak, but
674 statistically significant link to common ENSO indicators (Table 2). Increased synoptic activity at WDC is
675 linked to enhanced convection in the central and eastern tropical Pacific, which may be due to enhanced
676 frequency or intensity of El Niño events, or a mean climate state that is more El Niño-like; it seems likely
677 that the Pacific mean state and ENSO variability are strongly linked (Salau et al., 2012), and the distinction
678 may be irrelevant.

679 The key features of the WDC $^{86}\text{Kr}_{\text{xs}}$ record are compatible with paleo-ENSO changes commonly described
680 in the literature. A majority of Holocene ENSO reconstructions (Conroy et al., 2008; Driscoll et al., 2014;
681 Koutavas et al., 2006; Moy et al., 2002; Riedinger et al., 2002; Sadekov et al., 2013) and a wide range of
682 climate model simulations (Braconnot et al., 2012; Cane, 2005; Clement et al., 2000; Liu et al., 2000; Liu
683 et al., 2014; Zheng et al., 2008) all suggest weakened ENSO activity during the early and mid-Holocene, a
684 time with reduced WDC synoptic activity. For example, Fig. 7F shows the number of El Niño events per
685 century (with trend line) reconstructed from inorganic clastic laminae in sediments from Laguna
686 Pallacocha, Ecuador, a region strongly affected by ENSO (Moy et al., 2002). Likewise, it has been
687 suggested that the SST gradient between the West Pacific warm pool and East Pacific cold tongue was
688 enhanced during the mid-Holocene, perhaps indicating a more La Niña-like mean climate state (Koutavas
689 et al., 2002; Sadekov et al., 2013).

690 Going from the early Holocene to the Younger Dryas (YD), we observe a large increase in WDC synoptic
691 activity. Enhanced ENSO activity during Heinrich stadials is generally supported by climate model
692 simulations (Braconnot et al., 2012; Merkel et al., 2010; Timmermann et al., 2007), and by limited proxy
693 evidence for stadial periods more broadly (Stott et al., 2002). Enhanced ENSO variability during the

694 deglaciation is also found by Sadekov et al. (2013), although their record lacks the temporal resolution to
695 resolve the individual stages. The zonal SST gradient in the equatorial Pacific further reaches a minimum
696 during HS1, also consistent with higher El Niño intensity (Sadekov et al., 2013).

697 The observed variations in $^{86}\text{Kr}_{\text{xs}}$ and implied changes in WDC synoptic activity may thus have two
698 contributions: (1) ITCZ-driven changes to the South Pacific SPJ position, and (2) changes to ENSO activity.
699 Based on previous work, we argue these two amplify one another in driving WDC storminess, yet we expect
700 the former to make the larger contribution. To disentangle zonally-uniform changes to the SPJ from changes
701 specific to the Pacific sector (such as ENSO and the split jet), $^{86}\text{Kr}_{\text{xs}}$ records from different sectors of
702 Antarctica are needed. Replication of the deglacial and Holocene WDC $^{86}\text{Kr}_{\text{xs}}$ record presented here is also
703 a high priority, both at WDC itself and at the nearby SDM and RICE cores, to validate that the signals we
704 describe and interpret here are indeed real and regional in scale.

705 The position of the SHW during the LGM has been a topic of much scientific inquiry. Proxy data have been
706 interpreted to show a northward LGM shift of the SHW – with other scenarios, including no change at all,
707 not excluded by the data (Kohfeld et al., 2013). Such a shift is not supported by most climate models (Rojas
708 et al., 2009; Sime et al., 2013). Our $^{86}\text{Kr}_{\text{xs}}$ record suggests LGM synoptic activity in West Antarctica to be
709 comparable to today after accounting for site elevation effects (the elevation effect on $^{86}\text{Kr}_{\text{xs}}$ is within the
710 analytical error). This would be consistent with a Pacific SPJ position similar to today. Note that our site is
711 mostly sensitive to the position of the southern edge of the SPJ, and cannot meaningfully constrain changes
712 to the seasonality, width, and/or northern edge of the stormtracks. Therefore, it is not a-priori clear whether
713 our observations can be extrapolated to more general statements about SHW position and strength during
714 the LGM. Our data suggest that SPJ movement follows insolation and the ITCZ position, and hence the
715 LGM period may not be a good target for studying SHW movement in the first place given that it has a
716 precession index similar to the present-day.

717 Changes to the SPJ and its associated westerly surface winds have implications for ocean circulation and
718 marine productivity in the Southern Ocean via wind-driven upwelling. Opal flux records from the Antarctic
719 zone (Fig. 7G), reflecting diatom productivity, are commonly interpreted as a proxy for such upwelling –
720 with enhanced upwelling during southward displacement of the SHW (Anderson et al., 2009). Here we
721 only show records from the Pacific sector, given we find WDC $^{86}\text{Kr}_{\text{xs}}$ to reflect purely local SPJ dynamics
722 (Fig. 4A). Both published records suggest enhanced upwelling during the deglaciation (Fig. 7G), consistent
723 with a southward-shifted Pacific SPJ and enhanced storminess at WDC. The record from core PS75/072-4
724 (blue curve) further indicates an increasing productivity trend through the Holocene (Studer et al., 2018),
725 which is accompanied by a rise in surface nitrogen availability (reconstructed from diatom-bound nitrogen
726 isotopic composition, not shown); this Holocene trend matches our finding of increasing WDC storminess
727 and, by inference, an increasingly southern position of the Pacific SPJ and SHW. We thus conclude that
728 our interpretation of WDC $^{86}\text{Kr}_{\text{xs}}$ reflecting SPJ movement in parallel with the ITCZ, is broadly consistent
729 with indicators of wind-driven upwelling in the Pacific Antarctic zone.

730 **6 Conclusions**

731 Here we present a new gas-phase ice core climate proxy, Kr-86 excess, that reflects time-averaged surface
732 pressure variability at the site driven by synoptic activity. Surface pressure variability weakly disturbs the
733 gravitational settling and enrichment of the noble gas isotope ratios $\delta^{86}\text{Kr}$ and $\delta^{40}\text{Ar}$ via barometric
734 pumping. Owing to its higher diffusion coefficient, argon is less affected by this process than krypton is,
735 and therefore the difference $\delta^{86}\text{Kr}-\delta^{40}\text{Ar}$ is a measure of synoptic activity.

736 This interpretation is supported by a calibration study in which we measure $^{86}\text{Kr}_{\text{xs}}$ in late Holocene ice core
737 samples from eleven Antarctic and one Greenland ice core that represent a wide range of synoptic activity
738 in the modern climate. Two of the Antarctic cores were rejected due to clear evidence of refrozen melt
739 water. We find a strong correlation ($r = -0.94$ when using site mean data and $r = -0.83$ when using individual
740 samples, $p < 0.01$) between ice core $^{86}\text{Kr}_{\text{xs}}$ and barometric variability at the site, demonstrating the validity
741 of the new proxy.

742 Current limitations of the new $^{86}\text{Kr}_{\text{xs}}$ proxy are: (1) it requires relatively large and non-trivial corrections
743 for gas loss and thermal fractionation; (2) it is moderately sensitive to changes in convective zone thickness;
744 (3) firn air transport models cannot simulate the magnitude of $^{86}\text{Kr}_{\text{xs}}$ anomalies measured in ice samples;
745 (4) firn air samples show smaller $^{86}\text{Kr}_{\text{xs}}$ anomalies than ice samples from the same site do; (5) it may be
746 sensitive to the degree of density layering at the site, as a comparison of the nearby Law Dome DE08 and
747 DSSW20K cores suggests; (6) it does not work for warm sites that experience frequent melt; (7) the
748 measurement is challenging (with offsets observed between measurement campaigns), time consuming,
749 and needs large ice samples; and (8) long-term sample storage may impose data offsets. Due to these
750 limitations, we caution that any interpretation of temporal $^{86}\text{Kr}_{\text{xs}}$ changes remains speculative at present.

751 Using atmospheric reanalysis data, we show that synoptic-scale barometric variability in Antarctica is
752 primarily linked to the position and/or strength of the southern edge of the eddy-driven subpolar jet (SPJ,
753 also called polar front jet) with a southward SPJ displacement enhancing synoptic-scale surface pressure
754 variability in Antarctica. The commonly-defined modes of large-scale atmospheric variability, such as the
755 southern annular mode and the Pacific-South American pattern, impact Antarctic only weakly as they are
756 weighted towards the mid-latitudes; the exception is the Antarctic Peninsula, where synoptic activity is
757 well-correlated with the southern annular mode ($r = 0.68$). Sites in the Amundsen and Ross Sea sectors are
758 weakly linked to tropical Pacific climate and ENSO ($r = 0.31$ to $r = 0.43$).

759 We present a new record of $^{86}\text{Kr}_{\text{xs}}$ from the WAIS Divide ice core in West Antarctica, that covers the last
760 24ka including the LGM, deglaciation and Holocene. West Antarctic synoptic activity is slightly below
761 modern levels during the last glacial maximum (LGM); increases during the Heinrich Stadial 1 and Younger
762 Dryas North Atlantic cold periods; weakens abruptly at the Holocene onset; remains low during the early
763 and mid-Holocene (up to $\sim 17\%$ below modern), and gradually increases to its modern value. The WDC
764 $^{86}\text{Kr}_{\text{xs}}$ record resembles records of tropical hydrology and monsoon intensity that are commonly thought to
765 reflect the meridional position of the ITCZ; the sense of the correlation is that WDC synoptic activity is
766 weak when the ITCZ is in its northward position, and vice versa. We interpret the record to reflect
767 migrations of the eddy-driven SPJ in parallel with those of the ITCZ (Ceppi et al., 2013). Secondary
768 influences may come from tropical Pacific climate and ENSO activity. Our $^{86}\text{Kr}_{\text{xs}}$ record is consistent with
769 weakened ENSO activity (or a more La Niña-like mean state) during the mid- and early Holocene, and

770 enhanced ENSO activity during NH stadial periods – both these features have been described in the paleo-
771 ENSO literature. The inferred changes to the SPJ are broadly consistent with proxies that indicate enhanced
772 wind-driven upwelling in the Pacific Antarctic zone during NH cold stadial periods.

773 Kr-86 excess is a new and potentially useful ice core proxy with the ability to enhance our understanding
774 of past atmospheric circulation. More work to better understand this proxy is warranted, and presently the
775 conclusions of this paper should be considered as tentative. In particular, replication of the deglacial Kr-86
776 excess record presented here in nearby cores is needed before these results can be interpreted with
777 confidence. A full list of suggested follow-up studies is given in section 3.3. Despite the many challenges
778 of Kr-86 excess, its further development is worthwhile owing to the dearth of available proxies for
779 reconstructing SH extratropical atmospheric circulation.

780 Appendix A: data corrections

781 A1 Gas loss correction

782 Gas loss processes artificially enrich the $\delta^{40}\text{Ar}$ isotopic ratio used to calculate $^{86}\text{Kr}_{\text{xs}}$ (Kobashi et al., 2008b;
783 Severinghaus et al., 2009; Severinghaus et al., 2003). Figure A1B shows the relationships between the two
784 most common gas loss proxies $\delta\text{O}_2/\text{N}_2$ and $\delta\text{Ar}/\text{N}_2$ for all samples in the calibration dataset; we find a slope
785 close to the 2:1 slope commonly reported in the literature (Bender et al., 1995); the exception is the DE08-
786 OH site where the data fall on a 1:1 slope. Depletion in fugitive gases (such as O_2 and Ar) represents the
787 sum of losses during bubble closure in the firn (Bender, 2002; Huber et al., 2006; Severinghaus and Battle,
788 2006), and those during drilling, handling, storage, and analysis of the samples (Ikeda-Fukazawa et al.,
789 2005). The patterns are inconsistent with storage conditions alone – for example the DF and EDC cores
790 were stored very cold and SP drilled very recently; yet all three have strong $\delta\text{O}_2/\text{N}_2$ and $\delta\text{Ar}/\text{N}_2$ depletion.
791 Natural gas loss from the firn, as well as artefactual loss during drilling likely dominate the signal. The
792 DE08-OH samples were dry-drilled and suffered from poor ice quality for the most depleted samples, which
793 may explain the alternate 1:1 slope at the site (Appendix B); note though that a recent work suggests a ~5:1
794 slope for post-coring gas loss (Oyabu et al., 2021). The DE08-OH samples were also analyzed differently
795 from those at other sites, with $\delta\text{O}_2/\text{N}_2$ and $\delta\text{Ar}/\text{N}_2$ measurements performed on a separate smaller ice piece
796 (see section 2.2); the greater surface-to-volume ratio of such small samples may result in greater gas
797 fractionation while evacuating the sample flasks in the laboratory.

798 Severinghaus et al. (2009) hypothesize that the apparent 2:1 slope of $\delta\text{O}_2/\text{N}_2$ to $\delta\text{Ar}/\text{N}_2$ depletion is a
799 combination of two mechanisms: size-dependent fractionation during diffusion through the ice lattice, and
800 mass-dependent fractionation (such as molecular or Knudsen diffusion) within ice fractures. In this
801 interpretation, the exact slope would depend on the relative contribution of each process to the total gas
802 loss. It is improbable that both processes would occur in the same ratio at such a wide variety of sites; the
803 2:1 slope is thus more likely an attribute of the gas diffusion rate of gases through ice itself, which is strongly
804 size-dependent, and weakly mass-dependent (Battle et al., 2011).

805 Gas loss is well known to enrich ice samples in $\delta^{18}\text{O}-\text{O}_2$, and following Severinghaus et al. (2009) we plot
806 $\delta^{18}\text{O}$ (corrected for gravity and small atmospheric $\delta^{18}\text{O}_{\text{atm}}$ variations) against gravitationally-corrected
807 $\delta\text{O}_2/\text{N}_2$ in Fig. A1C. We find a slope of 3.5 per meg enrichment in $\delta^{18}\text{O}$ per ‰ of $\delta\text{O}_2/\text{N}_2$ gas loss. This is
808 less than values reported elsewhere (Severinghaus et al., 2009), but provides further evidence for mass-
809 dependent fractionation during gas loss. Our core top dataset further suggests a correlation between
810 $\delta^{40}\text{Ar} - 4 \times \delta^{15}\text{N}$ (a measure of $\delta^{40}\text{Ar}$ enrichment impacted by both thermal fractionation and gas loss) and
811 gravitationally corrected $\delta\text{Ar}/\text{N}_2$ (Fig. A1D), suggesting Ar loss leads to enrichment of the remaining $\delta^{40}\text{Ar}$.

812 Following Severinghaus et al. (2009), we assume that the $\delta^{40}\text{Ar}$ correction scales with gas loss indicator
813 $(\delta\text{O}_2/\text{N}_2 - \delta\text{Ar}/\text{N}_2)$:

$$814 \quad \Delta_{GL}^{40} = \varepsilon_{40} \times (\delta\text{O}_2/\text{N}_2 - \delta\text{Ar}/\text{N}_2)|_{\text{gravcorr}} \quad (\text{A1})$$

815 with Δ_{GL}^{40} the isotopic gas loss correction on $\delta^{40}\text{Ar}$ and ε_{40} a scaling parameter. Note that gravitationally
816 corrected $\delta\text{O}_2/\text{N}_2$ and $\delta\text{Ar}/\text{N}_2$ data are used. Here we rely on data from the Antarctic Byrd ice core for a best

817 estimate of ϵ_{40} (Fig. A2); some samples from this core suffered extreme gas loss with $(\delta O_2/N_2 - \delta Ar/N_2)$ as
 818 low as -100‰. This data set suggest $\epsilon_{40} = -0.008$, or 8 per meg $\delta^{40}Ar$ enrichment per ‰ of $(\delta O_2/N_2 - \delta Ar/N_2)$
 819 gas loss. Because of the 2:1 slope between $\delta O_2/N_2$ and $\delta Ar/N_2$, we find that $(\delta O_2/N_2 - \delta Ar/N_2) \approx \delta Ar/N_2$
 820 and therefore the coefficient ϵ_{40} would have a similar slope when regressed against $\delta Ar/N_2$ instead of
 821 $(\delta O_2/N_2 - \delta Ar/N_2)$.

822 The value of $\epsilon_{40} = -0.008$ agrees reasonably well with other studies. Kobashi et al. (2008) compare replicate
 823 sample pairs to back out gas loss, and find (statistically significant) correlations between $\delta^{40}Ar$ enrichment
 824 and $\delta Ar/N_2$ (again, which is similar to $\delta O_2/N_2 - \delta Ar/N_2$). Kobashi et al. (2008) find ϵ_{40} values of -0.006, -
 825 0.005 and +0.007, depending on the depth range and analytical campaign evaluated. The positive value is
 826 surprising, given that most observations, as well as theory, suggest ϵ_{40} should be negative – we consider
 827 this a spurious result given the weak $\delta^{40}Ar - \delta Ar/N_2$ correlation in that particular data set. The other two
 828 values of ϵ_{40} are in reasonable agreement with the Byrd value. For the Siple Dome ice core (Severinghaus
 829 et al., 2003), regressing $\delta^{40}Ar$ against $\delta Kr/Ar$ gives a slope of +0.007; this implies $\epsilon_{40} = -0.007$ in good
 830 agreement with our findings. Last, our coretop data suggest $\delta^{40}Ar$ enrichment with an ϵ_{40} value of -0.0072
 831 (Fig. A1D), also in good agreement with Byrd.

832 Given the uncertainty in the gas loss parameter, we verify that our results are valid for a wide range of ϵ_{40}
 833 values (Fig. 3B).

834 **A2 Thermal correction**

835 In the presence of a temperature gradient, thermal diffusion causes isotopic enrichment towards the colder
 836 location. The thermal diffusion sensitivity Ω in units of ‰K⁻¹ for the various gases is given as (Grachev
 837 and Severinghaus, 2003a, b; Kawamura et al., 2013):

$$838 \quad \Omega^{15} = \frac{8.656}{T} - \frac{1232}{T^2}$$

$$839 \quad \Omega^{40} = \frac{26.08}{T} - \frac{3952}{T^2}$$

$$840 \quad \Omega^{86} = \frac{5.05}{T} - \frac{580}{T^2}$$

841 We estimate the thermal gradient ΔT in the firn using N-15 excess (Severinghaus et al., 1998):

$$842 \quad \Delta T = \frac{{}^{15}N_{xs}}{\Omega^{15} - \Omega^{40}/4} = \frac{\delta^{15}N - (\delta^{40}Ar + \Delta_{GL}^{40})/4}{\Omega^{15} - \Omega^{40}/4} \quad (A2)$$

843 with Δ_{GL}^{40} the $\delta^{40}Ar$ gas loss correction from Eq. (A1). Positive values of ΔT indicate that the surface is
 844 warmer than the firn-ice transition. The ΔT then in turn allows us to estimate the thermal corrections:

$$845 \quad \Delta_{TF}^{15} = -\Omega^{15} \Delta T$$

$$\begin{aligned} \Delta_{TF}^{40} &= -\Omega^{40} \Delta T \\ \Delta_{TF}^{86} &= -\Omega^{86} \Delta T \end{aligned} \quad (\text{A3})$$

The samples from the calibration dataset are from the climatically stable late Holocene period, and typically close together in depth; the uncertainty in the ΔT estimation for individual samples therefore exceeds the temporal variability in ΔT . To reduce the uncertainty in the thermal correction we estimate ΔT for individual samples using Eq. (A2), and for each site average the available data to get a site-average firn temperature gradient $\overline{\Delta T}$. The thermal correction is then given by:

$$\begin{aligned} \Delta_{TF}^{15} &= -\Omega^{15} \overline{\Delta T} \\ \Delta_{TF}^{40} &= -\Omega^{40} \overline{\Delta T} \\ \Delta_{TF}^{86} &= -\Omega^{86} \overline{\Delta T} \end{aligned} \quad (\text{A4})$$

The two methods are compared in Figs. A3C (individual sample ΔT) and A3D (site mean $\overline{\Delta T}$); it is clear that the $\overline{\Delta T}$ approach reduces the spread in $^{86}\text{Kr}_{\text{xs}}$ (error bars), but not its mean (white dots). The ΔT estimates in individual samples are subject to errors in the isotopic measurements; some of these errors will cancel out in the $\overline{\Delta T}$.

For the downcore WDC record through the deglaciation we can no longer assume a stationary ΔT ; we instead rely on dynamic firn densification model simulations of ΔT (Buizert et al., 2015). A comparison of the simulated and data-based ΔT is shown in Fig. A5 for WDC. The data clearly show a lot more scatter/variability than the simulations do. We interpret this mainly as analytical noise in the $\delta^{15}\text{N}$ and $\delta^{40}\text{Ar}$ measurements, however, the gas loss correction (Appendix A1) also impacts the ΔT estimation in individual samples. The comparison suggests that the scatter in the ΔT estimates actually exceeds the magnitude of the simulated thermal signals. Using ΔT of the individual samples would thus introduce much scatter in the (thermally corrected) $^{86}\text{Kr}_{\text{xs}}$ records, and we choose to use the modelled ΔT instead.

868 **A3 Elevation correction**

To correct the deglacial WAIS Divide record for elevation changes, we here estimate the $^{86}\text{Kr}_{\text{xs}}$ dependence on site elevation using the calibration dataset. Note that elevation and synoptic activity are strongly correlated for the investigated sites ($r = -0.86$), with synoptic activity decreasing with elevation because the cyclonic systems do not penetrate deeply into the Antarctic interior. Figure A6 shows the result of this exercise. We find a slope of 34 per meg $\%^{-1}$ of $^{86}\text{Kr}_{\text{xs}}$ per 1000 m of elevation change, with a correlation of $r = 0.96$ when considering site-mean $^{86}\text{Kr}_{\text{xs}}$, and $r = 0.86$ when considering individual samples. Note that the GISP2 site is not included in the analysis because it is in Greenland where the elevation- $^{86}\text{Kr}_{\text{xs}}$ relationship may be different from Antarctica – it does however fit the Antarctic trend rather well. We further use the simulated WAIS Divide elevation history (Golledge et al., 2014), which simulates an LGM elevation of around 300 m higher than at present at WAIS Divide.

879 **Appendix B: Sub-annual $^{86}\text{Kr}_{\text{xs}}$ variations at DE08-OH**

880 The Law Dome DE08-OH site is a revisit of the DE08 site, drilled in the 2018/2019 Austral summer
881 Antarctic field season. We have samples from two separate cores: (1) thirteen 24-cm-long samples from a
882 10-cm-diameter core going from 97 m to 193 m depth at ~ 8 m sample spacing; and (2) eight 6-cm-long
883 samples from a 24-cm-diameter core going from 97.6 m to 99.8 m depth at 30 cm sample spacing. The
884 purpose of the first set was to determine possible long-term variations in $^{86}\text{Kr}_{\text{xs}}$; the purpose of the second
885 set to assess whether there are sub-annual variations in $^{86}\text{Kr}_{\text{xs}}$ due to the seasonality in firm properties and
886 bubble trapping.

887 Both cores were dry-drilled (i.e., no drill liquid was used). The 10-cm-diameter core used was drilled at the
888 beginning of the field season, the 24-cm-diameter core at the end of the field season. Prior to shipment off
889 the continent, both cores were stored in a chest freezer at Casey Station; due to a miscommunication this
890 freezer was set to -20°C rather than -26°C , yet the ice is believed to have stayed below -18°C .

891 Both DE08-OH cores experienced more gas loss than the original DE08 core that we also sampled (Fig.
892 A1 B). In particular the samples from the 10-cm-diameter core were strongly depleted in $\delta\text{Ar}/\text{N}_2$, with the
893 most extreme gas loss seen for the deepest samples where the ice quality was poorest.

894 Fig. B1 shows the high-resolution sub-annual DE08-OH sampling. The data were corrected for gas loss and
895 thermal fractionation, using a site-mean temperature gradient of $\overline{\Delta T} = -1.6^{\circ}\text{C}$, possibly related to a rectifier
896 effect (Morgan et al. 2022). We find strong (5-fold) variations in $^{86}\text{Kr}_{\text{xs}}$ on sub-annual time scales. With an
897 expected annual layer thickness of around 1.3 m at this depth, it appears as though there may be an annual-
898 scale variation in $^{86}\text{Kr}_{\text{xs}}$; the data set has insufficient length to establish this firmly.

899 We refrain from interpreting the long-term variations in $^{86}\text{Kr}_{\text{xs}}$ in the 10-cm-diameter core for two reasons.
900 First, given the strong sub-annual variations seen in the high-resolution sampling, it is unavoidable that we
901 are aliasing the underlying signal in the core. Second, the 10-cm-diameter core suffers from strong gas loss
902 (depleted $\delta\text{Ar}/\text{N}_2$). We attribute this primarily to the dry drilling and imperfect sample storage conditions.
903 Perhaps the greater stresses during drilling a 10-cm core (compared to the 24-cm diameter core) result in
904 more micro-fractures and gas loss.

905 **Supplement**

906 A data supplement is available with this paper.

907 **Data availability**

908 Data are available here: <https://www.usap-dc.org/view/project/p0010037>, and via the data supplement to
909 this paper.

910 **Author contributions**

911 CB, JS, AJS and EJB designed research; SS, AS, BB, KK, DB, AJS, JDM and IO contributed
912 measurements; KK, DME, NB, RLP, RB, EM-T, PDN, DT, and VVP contributed ice core samples; CB
913 and WHGR analyzed reanalysis data; CB, AJS, and BB performed firm modelling; CB drafted the
914 manuscript with input from all authors.

915 **Competing Interests**

916 The authors declare no competing interests.

917 **Acknowledgements**

918 The idea for the Kr-86 excess proxy came out of discussions at the 2014 WAIS Divide Ice Core Science
919 Meeting held at Scripps Institution of Oceanography in La Jolla, CA. The authors want to thank John
920 Chiang, Justin Wettstein, Zanna Chase, Bob Anderson, Tyler Jones and Eric Steig for useful discussions,
921 data sharing and manuscript feedback, the NSF ice core facility (NSF-ICF, formerly the National Ice Core
922 Laboratory) for curating and distributing ice core samples, the European Centre for Medium-Range
923 Weather Forecasts (ECMWF) for making ERA-Interim reanalysis datasets publicly available, and the US
924 ice drilling program for coordinating ice core drilling in Antarctica. Ice drilling and field support at Law
925 Dome and sample handling in Hobart was provided by the Australian Antarctic Science Program, the
926 Australian Antarctic Division and (at DE08-OH) the U.S. National Science Foundation.

927 **Financial Support**

928 We gratefully acknowledge financial support from the U.S. National Science Foundation (grant numbers
929 ANT-0944343, ANT-1543267, ANT-1543229, ANT-1643716 and ANT-1643669), the New Zealand
930 Ministry of Business, Innovation and Employment (grant numbers RDF-VUW-1103, 15-VUW-131,
931 540GCT32).

932 **References**

- 933 Anderson, R.F., Ali, S., Bradtmiller, L.I., Nielsen, S.H.H., Fleisher, M.Q., Anderson, B.E. and Burckle, L.H. (2009)
 934 Wind-Driven Upwelling in the Southern Ocean and the Deglacial Rise in Atmospheric CO₂. *Science* 323, 1443-
 935 1448.
- 936 Baggenstos, D., Häberli, M., Schmitt, J., Shackleton, S.A., Birner, B., Severinghaus, J.P., Kellerhals, T. and Fischer,
 937 H. (2019) Earth's radiative imbalance from the Last Glacial Maximum to the present. *Proc. Natl. Acad. Sci. U. S.*
 938 *A.*, 201905447.
- 939 Bals-Elsholz, T.M., Atallah, E.H., Bosart, L.F., Wasula, T.A., Cempa, M.J. and Lupo, A.R. (2001) The Wintertime
 940 Southern Hemisphere Split Jet: Structure, Variability, and Evolution. *J. Clim.* 14, 4191-4215.
- 941 Battle, M.O., Severinghaus, J.P., Sofen, E.D., Plotkin, D., Orsi, A.J., Aydin, M., Montzka, S.A., Sowers, T. and Tans,
 942 P.P. (2011) Controls on the movement and composition of firn air at the West Antarctic Ice Sheet Divide. *Atmos.*
 943 *Chem. Phys.* 11, 11007-11021.
- 944 Bender, M., Sowers, T. and Lipenkov, V. (1995) ON THE CONCENTRATIONS OF O-2, N-2, AND AR IN
 945 TRAPPED GASES FROM ICE CORES. *J. Geophys. Res.* 100, 18651-18660.
- 946 Bender, M.L. (2002) Orbital tuning chronology for the Vostok climate record supported by trapped gas composition.
 947 *Earth Planet. Sci. Lett.* 204, 275-289.
- 948 Bereiter, B., Kawamura, K. and Severinghaus, J.P. (2018a) New methods for measuring atmospheric heavy noble gas
 949 isotope and elemental ratios in ice core samples. *Rapid communications in mass spectrometry* 32, 801-814.
- 950 Bereiter, B., Shackleton, S., Baggenstos, D., Kawamura, K. and Severinghaus, J. (2018b) Mean global ocean
 951 temperatures during the last glacial transition. *Nature* 553, 39.
- 952 Birner, B., Buizert, C., Wagner, T.J.W. and Severinghaus, J.P. (2018) The influence of layering and barometric
 953 pumping on firn air transport in a 2-D model. *The Cryosphere* 12, 2021-2037.
- 954 Braconnot, P., Luan, Y., Brewer, S. and Zheng, W. (2012) Impact of Earth's orbit and freshwater fluxes on Holocene
 955 climate mean seasonal cycle and ENSO characteristics. *Clim. Dyn.* 38, 1081-1092.
- 956 Broccoli, A.J., Dahl, K.A. and Stouffer, R.J. (2006) Response of the ITCZ to Northern Hemisphere cooling. *Geophys.*
 957 *Res. Lett.* 33, L01702.
- 958 Buizert, C., Cuffey, K.M., Severinghaus, J.P., Baggenstos, D., Fudge, T.J., Steig, E.J., Markle, B.R., Winstrup, M.,
 959 Rhodes, R.H., Brook, E.J., Sowers, T.A., Clow, G.D., Cheng, H., Edwards, L.R., Sigl, M., McConnell, J.R. and
 960 Taylor, K.C. (2015) The WAIS Divide deep ice core WD2014 chronology - part 1: Methane synchronization (68-
 961 31 ka BP) and the gas age-ice age difference. *Climate of the Past* 11, 153-173.
- 962 Buizert, C. and Severinghaus, J.P. (2016) Dispersion in deep polar firn driven by synoptic-scale surface pressure
 963 variability. *The Cryosphere* 10, 2099-2111.
- 964 Buizert, C., Sigl, M., Severi, M., Markle, B.R., Wettstein, J.J., McConnell, J.R., Pedro, J.B., Sodemann, H., Goto-
 965 Azuma, K., Kawamura, K., Fujita, S., Motoyama, H., Hirabayashi, M., Uemura, R., Stenni, B., Parrenin, F., He,
 966 F., Fudge, T.J. and Steig, E.J. (2018) Abrupt ice-age shifts in southern westerly winds and Antarctic climate forced
 967 from the north. *Nature* 563, 681-685.
- 968 Buizert, C., Sowers, T. and Blunier, T. (2013) Assessment of diffusive isotopic fractionation in polar firn, and
 969 application to ice core trace gas records. *Earth Planet. Sci. Lett.* 361, 110-119.
- 970 Cai, W., Santoso, A., Wang, G., Yeh, S.-W., An, S.-I., Cobb, K.M., Collins, M., Guilyardi, E., Jin, F.-F., Kug, J.-S.,
 971 Lengaigne, M., McPhaden, M.J., Takahashi, K., Timmermann, A., Vecchi, G., Watanabe, M. and Wu, L. (2015)
 972 ENSO and greenhouse warming. *Nature Clim. Change* 5, 849-859.
- 973 Cane, M.A. (2005) The evolution of El Niño, past and future. *Earth Planet. Sci. Lett.* 230, 227-240.
- 974 Ceppi, P., Hwang, Y.-T., Liu, X., Frierson, D.M.W. and Hartmann, D.L. (2013) The relationship between the ITCZ
 975 and the Southern Hemispheric eddy-driven jet. *J. Geophys. Res.* 118, 5136-5146.
- 976 Chase, Z., Anderson, R.F., Fleisher, M.Q. and Kubik, P.W. (2003) Accumulation of biogenic and lithogenic material
 977 in the Pacific sector of the Southern Ocean during the past 40,000 years. *Deep Sea Research Part II: Topical Studies*
 978 *in Oceanography* 50, 799-832.
- 979 Cheng, H., Edwards, R.L., Sinha, A., Spötl, C., Yi, L., Chen, S., Kelly, M., Kathayat, G., Wang, X., Li, X., Kong, X.,
 980 Wang, Y., Ning, Y. and Zhang, H. (2016) The Asian monsoon over the past 640,000 years and ice age terminations.
 981 *Nature* 534, 640-646.
- 982 Chiang, J.C. and Friedman, A.R. (2012) Extratropical cooling, interhemispheric thermal gradients, and tropical
 983 climate change. *Annu. Rev. Earth Planet. Sci.* 40, 383-412.
- 984 Chiang, J.C.H. and Bitz, C.M. (2005) Influence of high latitude ice cover on the marine Intertropical Convergence
 985 Zone. *Clim. Dyn.* 25, 477-496.

986 Chiang, J.C.H., Lee, S.-Y., Putnam, A.E. and Wang, X. (2014) South Pacific Split Jet, ITCZ shifts, and atmospheric
987 North–South linkages during abrupt climate changes of the last glacial period. *Earth Planet. Sci. Lett.* 406, 233-
988 246.

989 Clement, A.C., Seager, R. and Cane, M.A. (2000) Suppression of El Niño during the Mid-Holocene by changes in the
990 Earth's orbit. *Paleoceanography* 15, 731-737.

991 Cobb, K.M., Westphal, N., Sayani, H.R., Watson, J.T., Di Lorenzo, E., Cheng, H., Edwards, R.L. and Charles, C.D.
992 (2013) Highly Variable El Niño–Southern Oscillation Throughout the Holocene. *Science* 339, 67-70.

993 Conroy, J.L., Overpeck, J.T., Cole, J.E., Shanahan, T.M. and Steinitz-Kannan, M. (2008) Holocene changes in eastern
994 tropical Pacific climate inferred from a Galápagos lake sediment record. *Quat. Sci. Rev.* 27, 1166-1180.

995 Cruz, F.W., Burns, S.J., Karmann, I., Sharp, W.D., Vuille, M., Cardoso, A.O., Ferrari, J.A., Dias, P.L.S. and Viana,
996 O. (2005) Insolation-driven changes in atmospheric circulation over the past 116,000 years in subtropical Brazil.
997 *Nature* 434, 63-66.

998 Dee, D.P., Uppala, S.M., Simmons, A.J., Berrisford, P., Poli, P., Kobayashi, S., Andrae, U., Balmaseda, M.A.,
999 Balsamo, G., Bauer, P., Bechtold, P., Beljaars, A.C.M., van de Berg, L., Bidlot, J., Bormann, N., Delsol, C.,
1000 Dragani, R., Fuentes, M., Geer, A.J., Haimberger, L., Healy, S.B., Hersbach, H., Hólm, E.V., Isaksen, I., Kållberg,
1001 P., Köhler, M., Matricardi, M., McNally, A.P., Monge-Sanz, B.M., Morcrette, J.J., Park, B.K., Peubey, C., de
1002 Rosnay, P., Tavolato, C., Thépaut, J.N. and Vitart, F. (2011) The ERA-Interim reanalysis: configuration and
1003 performance of the data assimilation system. *Quarterly Journal of the Royal Meteorological Society* 137, 553-597.

1004 Driscoll, R., Elliot, M., Russon, T., Welsh, K., Yokoyama, Y. and Tudhope, A. (2014) ENSO reconstructions over the
1005 past 60 ka using giant clams (*Tridacna* sp.) from Papua New Guinea. *Geophys. Res. Lett.* 41, 6819-6825.

1006 Dykoski, C.A., Edwards, R.L., Cheng, H., Yuan, D.X., Cai, Y.J., Zhang, M.L., Lin, Y.S., Qing, J.M., An, Z.S. and
1007 Revenaugh, J. (2005) A high-resolution, absolute-dated Holocene and deglacial Asian monsoon record from
1008 Dongge Cave, China. *Earth Planet. Sci. Lett.* 233, 71-86.

1009 Emile-Geay, J., Cobb, K.M., Carré, M., Braconnot, P., Leloup, J., Zhou, Y., Harrison, S.P., Corrège, T., McGregor,
1010 H.V., Collins, M., Driscoll, R., Elliot, M., Schneider, B. and Tudhope, A. (2015) Links between tropical Pacific
1011 seasonal, interannual and orbital variability during the Holocene. *Nat. Geosci.* 9, 168.

1012 Etheridge, D.M., Pearman, G.I. and Fraser, P.J. (1992) CHANGES IN TROPOSPHERIC METHANE BETWEEN
1013 1841 AND 1978 FROM A HIGH ACCUMULATION-RATE ANTARCTIC ICE CORE. *Tellus* 44, 282-294.

1014 Fahnestock, M.A., Scambos, T.A., Shuman, C.A., Arthern, R.J., Winebrenner, D.P. and Kwok, R. (2000) Snow
1015 megadune fields on the East Antarctic Plateau: Extreme atmosphere-ice interaction. *Geophys. Res. Lett.* 27, 3719-
1016 3722.

1017 Fowler, A.M., Boswijk, G., Lorrey, A.M., Gergis, J., Pirie, M., McCloskey, S.P.J., Palmer, J.G. and Wunder, J. (2012)
1018 Multi-centennial tree-ring record of ENSO-related activity in New Zealand. *Nature Climate Change* 2, 172.

1019 Fujita, S., Okuyama, J., Hori, A. and Hondoh, T. (2009) Metamorphism of stratified firn at Dome Fuji, Antarctica: A
1020 mechanism for local insolation modulation of gas transport conditions during bubble close off. *J. Geophys. Res.*
1021 114.

1022 Gergis, J.L. and Fowler, A.M. (2009) A history of ENSO events since A.D. 1525: implications for future climate
1023 change. *Clim. Change* 92, 343-387.

1024 Golledge, N.R., Meniel, L., Carter, L., Fogwill, C.J., England, M.H., Cortese, G. and Levy, R.H. (2014) Antarctic
1025 contribution to meltwater pulse 1A from reduced Southern Ocean overturning. *Nat Comm.* 5, 5107.

1026 Grachev, A.M. and Severinghaus, J.P. (2003a) Determining the thermal diffusion factor for Ar-40/Ar-36 in air to aid
1027 paleoreconstruction of abrupt climate change. *J. Phys. Chem. A* 107, 4636-4642.

1028 Grachev, A.M. and Severinghaus, J.P. (2003b) Laboratory determination of thermal diffusion constants for N-
1029 29(2)/N-28(2) in air at temperatures from -60 to 0 degrees C for reconstruction of magnitudes of abrupt climate
1030 changes using the ice core fossil-air paleothermometer. *Geochim. Cosmochim. Acta* 67, 345-360.

1031 Grootes, P.M., Stuiver, M., White, J.W.C., Johnsen, S. and Jouzel, J. (1993) Comparison of oxygen isotope records
1032 from the GISP2 and GRIP Greenland ice cores. *Nature* 366, 552-554.

1033 Headly, M.A. and Severinghaus, J.P. (2007) A method to measure Kr/N-2 ratios in air bubbles trapped in ice cores
1034 and its application in reconstructing past mean ocean temperature. *J. Geophys. Res.* 112, 12.

1035 Herron, M.M. and Langway, C.C. (1980) Firn densification: An empirical model. *J. Glaciol.* 25, 373-385.

1036 Huang, B., Banzon, V.F., Freeman, E., Lawrimore, J., Liu, W., Peterson, T.C., Smith, T.M., Thorne, P.W., Woodruff,
1037 S.D. and Zhang, H.-M. (2014) Extended Reconstructed Sea Surface Temperature Version 4 (ERSST.v4). Part I:
1038 Upgrades and Intercomparisons. *J. Clim.* 28, 911-930.

1039 Huber, C., Beyerle, U., Leuenberger, M., Schwander, J., Kipfer, R., Spahni, R., Severinghaus, J.P. and Weiler, K.
1040 (2006) Evidence for molecular size dependent gas fractionation in firn air derived from noble gases, oxygen, and
1041 nitrogen measurements. *Earth Planet. Sci. Lett.* 243, 61-73.

1042 Ikeda-Fukazawa, T., Fukumizu, K., Kawamura, K., Aoki, S., Nakazawa, T. and Hondoh, T. (2005) Effects of
1043 molecular diffusion on trapped gas composition in polar ice cores. *Earth Planet. Sci. Lett.* 229, 183-192.

1044 Kanner, L.C., Burns, S.J., Cheng, H. and Edwards, R.L. (2012) High-Latitude Forcing of the South American Summer
1045 Monsoon During the Last Glacial. *Science* 335, 570-573

1046 Kawamura, K., Severinghaus, J.P., Albert, M.R., Courville, Z.R., Fahnestock, M.A., Scambos, T., Shields, E. and
1047 Shuman, C.A. (2013) Kinetic fractionation of gases by deep air convection in polar firn. *Atmos. Chem. Phys.* 13,
1048 11141-11155.

1049 Kawamura, K., Severinghaus, J.P., Ishidoya, S., Sugawara, S., Hashida, G., Motoyama, H., Fujii, Y., Aoki, S. and
1050 Nakazawa, T. (2006) Convective mixing of air in firn at four polar sites. *Earth Planet. Sci. Lett.* 244, 672-682.

1051 Kobashi, T., Severinghaus, J.P. and Barnola, J.M. (2008a) 4 +/- 1.5 degrees C abrupt warming 11,270 yr ago identified
1052 from trapped air in Greenland ice. *Earth Planet. Sci. Lett.* 268, 397-407.

1053 Kobashi, T., Severinghaus, J.P. and Kawamura, K. (2008b) Argon and nitrogen isotopes of trapped air in the GISP2
1054 ice core during the Holocene epoch (0-11,500 B.P.): Methodology and implications for gas loss processes.
1055 *Geochim. Cosmochim. Acta* 72, 4675-4686.

1056 Kohfeld, K.E., Graham, R.M., de Boer, A.M., Sime, L.C., Wolff, E.W., Le Quéré, C. and Bopp, L. (2013) Southern
1057 Hemisphere westerly wind changes during the Last Glacial Maximum: paleo-data synthesis. *Quat. Sci. Rev.* 68,
1058 76-95.

1059 Koutavas, A., deMenocal, P.B., Olive, G.C. and Lynch-Stieglitz, J. (2006) Mid-Holocene El Niño–Southern
1060 Oscillation (ENSO) attenuation revealed by individual foraminifera in eastern tropical Pacific sediments. *Geology*
1061 34, 993-996.

1062 Koutavas, A., Lynch-Stieglitz, J., Marchitto, T.M. and Sachs, J.P. (2002) El Niño-Like Pattern in Ice Age Tropical
1063 Pacific Sea Surface Temperature. *Science* 297, 226-230.

1064 Lamy, F., Chiang, J.C.H., Martínez-Méndez, G., Thierens, M., Arz, H.W., Bosmans, J., Hebbeln, D., Lambert, F.,
1065 Lembke-Jene, L. and Stuut, J.-B. (2019) Precession modulation of the South Pacific westerly wind belt over the
1066 past million years. *Proc. Natl. Acad. Sci. U. S. A.*, 201905847.

1067 Lee, S. and Kim, H.-k. (2003) The Dynamical Relationship between Subtropical and Eddy-Driven Jets. *Journal of the*
1068 *Atmospheric Sciences* 60, 1490-1503.

1069 Lee, S.Y., Chiang, J.C., Matsumoto, K. and Tokos, K.S. (2011) Southern Ocean wind response to North Atlantic
1070 cooling and the rise in atmospheric CO₂: Modeling perspective and paleoceanographic implications.
1071 *Paleoceanography* 26.

1072 Liu, Z., Kutzbach, J. and Wu, L. (2000) Modeling climate shift of El Niño variability in the Holocene. *Geophys. Res.*
1073 *Lett.* 27, 2265-2268.

1074 Liu, Z., Lu, Z., Wen, X., Otto-Bliessner, B.L., Timmermann, A. and Cobb, K.M. (2014) Evolution and forcing
1075 mechanisms of El Niño over the past 21,000 years. *Nature* 515, 550-553.

1076 Lynch-Stieglitz, J. (2017) The Atlantic Meridional Overturning Circulation and Abrupt Climate Change. *Annual*
1077 *Review of Marine Science* 9, 83-104.

1078 Mantua, N.J. and Hare, S.R. (2002) The Pacific Decadal Oscillation. *Journal of Oceanography* 58, 35-44.

1079 Marcott, S.A., Shakun, J.D., Clark, P.U. and Mix, A.C. (2013) A Reconstruction of Regional and Global Temperature
1080 for the Past 11,300 Years. *Science* 339, 1198-1201.

1081 Marino, G., Zahn, R., Ziegler, M., Purcell, C., Knorr, G., Hall, I.R., Ziveri, P. and Elderfield, H. (2013) Agulhas salt-
1082 leakage oscillations during abrupt climate changes of the Late Pleistocene. *Paleoceanography* 28, 599-606.

1083 Markle, B.R., Steig, E.J., Buizert, C., Schoenemann, S.W., Bitz, C.M., Fudge, T.J., Pedro, J.B., Ding, Q., Jones, T.R.,
1084 White, J.W.C. and Sowers, T. (2017) Global atmospheric teleconnections during Dansgaard-Oeschger events.
1085 *Nature Geosci* 10, 36-40.

1086 Marshall, J. and Speer, K. (2012) Closure of the meridional overturning circulation through Southern Ocean
1087 upwelling. *Nature Geosci* 5, 171-180.

1088 McGee, D., Donohoe, A., Marshall, J. and Ferreira, D. (2014) Changes in ITCZ location and cross-equatorial heat
1089 transport at the Last Glacial Maximum, Heinrich Stadial 1, and the mid-Holocene. *Earth Planet. Sci. Lett.* 390, 69-
1090 79.

1091 Merkel, U., Prange, M. and Schulz, M. (2010) ENSO variability and teleconnections during glacial climates. *Quat.*
1092 *Sci. Rev.* 29, 86-100.

1093 Mo, K.C. and Paegle, J.N. (2001) The Pacific–South American modes and their downstream effects. *International*
1094 *Journal of Climatology* 21, 1211-1229.

1095 Moy, C.M., Seltzer, G.O., Rodbell, D.T. and Anderson, D.M. (2002) Variability of El Niño/Southern Oscillation
1096 activity at millennial timescales during the Holocene epoch. *Nature* 420, 162.

1097 Nakamura, H. and Shimpo, A. (2004) Seasonal Variations in the Southern Hemisphere Storm Tracks and Jet Streams
1098 as Revealed in a Reanalysis Dataset. *J. Clim.* 17, 1828-1844.

1099 Orsi, A.J., Kawamura, K., Fegyveresi, J.M., Headly, M.A., Alley, R.B. and Severinghaus, J.P. (2015) Differentiating
1100 bubble-free layers from melt layers in ice cores using noble gases. *J. Glaciol.* 61, 585-594.

1101 Oyabu, I., Kawamura, K., Uchida, T., Fujita, S., Kitamura, K., Hirabayashi, M., Aoki, S., Morimoto, S., Nakazawa,
1102 T., Severinghaus, J.P. and Morgan, J.D. (2021) Fractionation of O₂N₂ and ArN₂ in the Antarctic ice sheet during
1103 bubble formation and bubble-clathrate hydrate transition from precise gas measurements of the Dome Fuji ice
1104 core. *The Cryosphere* 15, 5529-5555.

1105 Parkinson, C.L. and Cavalieri, D.J. (2012) Antarctic sea ice variability and trends, 1979–2010. *The Cryosphere*
1106 6, 871-880.

1107 Pedro, J.B., Jochum, M., Buizert, C., He, F., Barker, S. and Rasmussen, S.O. (2018) Beyond the bipolar seesaw:
1108 Toward a process understanding of interhemispheric coupling. *Quat. Sci. Rev.* 192, 27-46.

1109 Peterson, L.C., Haug, G.H., Hughen, K.A. and Röhl, U. (2000) Rapid Changes in the Hydrologic Cycle of the Tropical
1110 Atlantic During the Last Glacial. *Science* 290, 1947-1951.

1111 Rahmstorf, S. (2002) Ocean circulation and climate during the past 120,000 years. *Nature* 419, 207-214.

1112 Raynaud, D., Lipenkov, V., Lemieux-Dudon, B., Duval, P., Loutre, M.F. and Lhomme, N. (2007) The local insolation
1113 signature of air content in Antarctic ice. A new step toward an absolute dating of ice records. *Earth Planet. Sci.*
1114 *Lett.* 261, 337-349.

1115 Rein, B., Lückge, A., Reinhardt, L., Sirocko, F., Wolf, A. and Dullo, W.-C. (2005) El Niño variability off Peru during
1116 the last 20,000 years. *Paleoceanography* 20.

1117 Rhodes, R.H., Fain, X., Brook, E.J., McConnell, J.R., Maselli, O.J., Sigl, M., Edwards, J., Buizert, C., Blunier, T.,
1118 Chappellaz, J. and Freitag, J. (2016) Local artifacts in ice core methane records caused by layered bubble trapping
1119 and in situ production: a multi-site investigation. *Clim. Past* 12, 1061-1077.

1120 Riedinger, M.A., Steinitz-Kannan, M., Last, W.M. and Brenner, M. (2002) A ~6100 14C yr record of El Niño activity
1121 from the Galápagos Islands. *Journal of Paleolimnology* 27, 1-7.

1122 Rind, D., Russell, G., Schmidt, G., Sheth, S., Collins, D., Demenocal, P. and Teller, J. (2001) Effects of glacial
1123 meltwater in the GISS coupled atmosphere-ocean model: 2. A bipolar seesaw in Atlantic Deep Water production.
1124 *Journal of Geophysical Research: Atmospheres* (1984–2012) 106, 27355-27365.

1125 Rojas, M., Moreno, P., Kageyama, M., Crucifix, M., Hewitt, C., Abe-Ouchi, A., Ohgaito, R., Brady, E.C. and Hope,
1126 P. (2009) The Southern Westerlies during the last glacial maximum in PMIP2 simulations. *Clim. Dyn.* 32, 525-
1127 548.

1128 Russell, J.L., Dixon, K.W., Gnanadesikan, A., Stouffer, R.J. and Toggweiler, J.R. (2006) The Southern Hemisphere
1129 Westerlies in a Warming World: Propping Open the Door to the Deep Ocean. *J. Clim.* 19, 6382-6390.

1130 Sadekov, A.Y., Ganeshram, R., Pichevin, L., Berdin, R., McClymont, E., Elderfield, H. and Tudhope, A.W. (2013)
1131 Palaeoclimate reconstructions reveal a strong link between El Niño-Southern Oscillation and Tropical Pacific mean
1132 state. *Nature Communications* 4, 2692.

1133 Salau, O., Schneider, B., Park, W., Khon, V. and Latif, M. (2012) Modeling the ENSO impact of orbitally induced
1134 mean state climate changes. *J. Geophys. Res.* 117.

1135 Schaller, C.F., Freitag, J. and Eisen, O. (2017) Critical porosity of gas enclosure in polar firn independent of climate.
1136 *Clim. Past* 13, 1685-1693.

1137 Schneider, T., Bischoff, T. and Haug, G.H. (2014) Migrations and dynamics of the intertropical convergence zone.
1138 *Nature* 513, 45-53.

1139 Schwander, J. (1989) The transformation of snow to ice and the occlusion of gases in: Oescher, H., Langway, C.C.
1140 (Eds.), *The Environmental record in glaciers and ice sheets*. John Wiley, New York, pp. 53-67.

1141 Schwander, J., Barnola, J.M., Andrie, C., Leuenberger, M., Ludin, A., Raynaud, D. and Stauffer, B. (1993) THE AGE
1142 OF THE AIR IN THE FIRN AND THE ICE AT SUMMIT, GREENLAND. *J. Geophys. Res.* 98, 2831-2838.

1143 Schwander, J., Stauffer, B. and Sigg, A. (1988) Air mixing in firn and the age of the air at pore close-off, *Annals of*
1144 *Glaciology*, pp. 141-145.

1145 Severinghaus, J.P., Albert, M.R., Courville, Z.R., Fahnestock, M.A., Kawamura, K., Montzka, S.A., Muhle, J.,
1146 Scambos, T.A., Shields, E., Shuman, C.A., Suwa, M., Tans, P. and Weiss, R.F. (2010) Deep air convection in the
1147 firn at a zero-accumulation site, central Antarctica. *Earth Planet. Sci. Lett.* 293, 359-367.

1148 Severinghaus, J.P. and Battle, M.O. (2006) Fractionation of gases in polar ice during bubble close-off: New constraints
1149 from firn air Ne, Kr and Xe observations. *Earth Planet. Sci. Lett.* 244, 474-500.

1150 Severinghaus, J.P., Beaudette, R., Headly, M.A., Taylor, K. and Brook, E.J. (2009) Oxygen-18 of O₂ Records the
1151 Impact of Abrupt Climate Change on the Terrestrial Biosphere. *Science* 324, 1431-1434.

1152 Severinghaus, J.P., Grachev, A., Luz, B. and Caillon, N. (2003) A method for precise measurement of argon 40/36
1153 and krypton/argon ratios in trapped air in polar ice with applications to past firn thickness and abrupt climate
1154 change in Greenland and at Siple Dome, Antarctica. *Geochim. Cosmochim. Acta* 67, 325-343.

1155 Severinghaus, J.P., Sowers, T., Brook, E.J., Alley, R.B. and Bender, M.L. (1998) Timing of abrupt climate change at
1156 the end of the Younger Dryas interval from thermally fractionated gases in polar ice. *Nature* 391, 141-146.

1157 Shakun, J.D., Clark, P.U., He, F., Marcott, S.A., Mix, A.C., Liu, Z., Otto-Bliesner, B., Schmittner, A. and Bard, E.
1158 (2012) Global warming preceded by increasing carbon dioxide concentrations during the last deglaciation. *Nature*
1159 484, 49-54.

1160 Sime, L.C., Kohfeld, K.E., Le Quéré, C., Wolff, E.W., de Boer, A.M., Graham, R.M. and Bopp, L. (2013) Southern
1161 Hemisphere westerly wind changes during the Last Glacial Maximum: model-data comparison. *Quat. Sci. Rev.*
1162 64, 104-120.

1163 Simpson, I.R., Hitchcock, P., Shepherd, T.G. and Scinocca, J.F. (2011) Stratospheric variability and tropospheric
1164 annular-mode timescales. *Geophys. Res. Lett.* 38.

1165 Sowers, T., Bender, M., Raynaud, D. and Korotkevich, Y.S. (1992) $\delta^{15}\text{N}$ of N_2 in air trapped in polar ice: A tracer
1166 of gas transport in the firn and a possible constraint on ice age-gas age differences. *J. Geophys. Res.* 97, 15683-
1167 15697.

1168 Stott, L., Poulsen, C., Lund, S. and Thunell, R. (2002) Super ENSO and Global Climate Oscillations at Millennial
1169 Time Scales. *Science* 297, 222-226.

1170 Studer, A.S., Sigman, D.M., Martínez-García, A., Benz, V., Winckler, G., Kuhn, G., Esper, O., Lamy, F., Jaccard,
1171 S.L., Wacker, L., Oleynik, S., Gersonde, R. and Haug, G.H. (2015) Antarctic Zone nutrient conditions during the
1172 last two glacial cycles. *Paleoceanography* 30, 2014PA002745.

1173 Studer, A.S., Sigman, D.M., Martínez-García, A., Thöle, L.M., Michel, E., Jaccard, S.L., Lippold, J.A., Mazaud, A.,
1174 Wang, X.T., Robinson, L.F., Adkins, J.F. and Haug, G.H. (2018) Increased nutrient supply to the Southern Ocean
1175 during the Holocene and its implications for the pre-industrial atmospheric CO_2 rise. *Nat. Geosci.* 11, 756-760.

1176 Thomas, E.R., Marshall, G.J. and McConnell, J.R. (2008) A doubling in snow accumulation in the western Antarctic
1177 Peninsula since 1850. *Geophys. Res. Lett.* 35.

1178 Thompson, D.W.J. and Wallace, J.M. (2000) Annular Modes in the Extratropical Circulation. Part I: Month-to-Month
1179 Variability*. *J. Clim.* 13, 1000-1016.

1180 Thompson, L.G., Mosley-Thompson, E., Davis, M.E., Zagorodnov, V.S., Howat, I.M., Mikhailenko, V.N. and Lin, P.-
1181 N. (2013) Annually Resolved Ice Core Records of Tropical Climate Variability over the Past ~1800 Years. *Science*
1182 340, 945-950.

1183 Timmermann, A., Okumura, Y., An, S.I., Clement, A., Dong, B., Guilyardi, E., Hu, A., Jungclaus, J.H., Renold, M.,
1184 Stocker, T.F., Stouffer, R.J., Sutton, R., Xie, S.P. and Yin, J. (2007) The Influence of a Weakening of the Atlantic
1185 Meridional Overturning Circulation on ENSO. *J. Clim.* 20, 4899-4919.

1186 Toggweiler, J.R., Russell, J.L. and Carson, S.R. (2006) Midlatitude westerlies, atmospheric CO_2 , and climate change
1187 during the ice ages. *Paleoceanography* 21, PA2005.

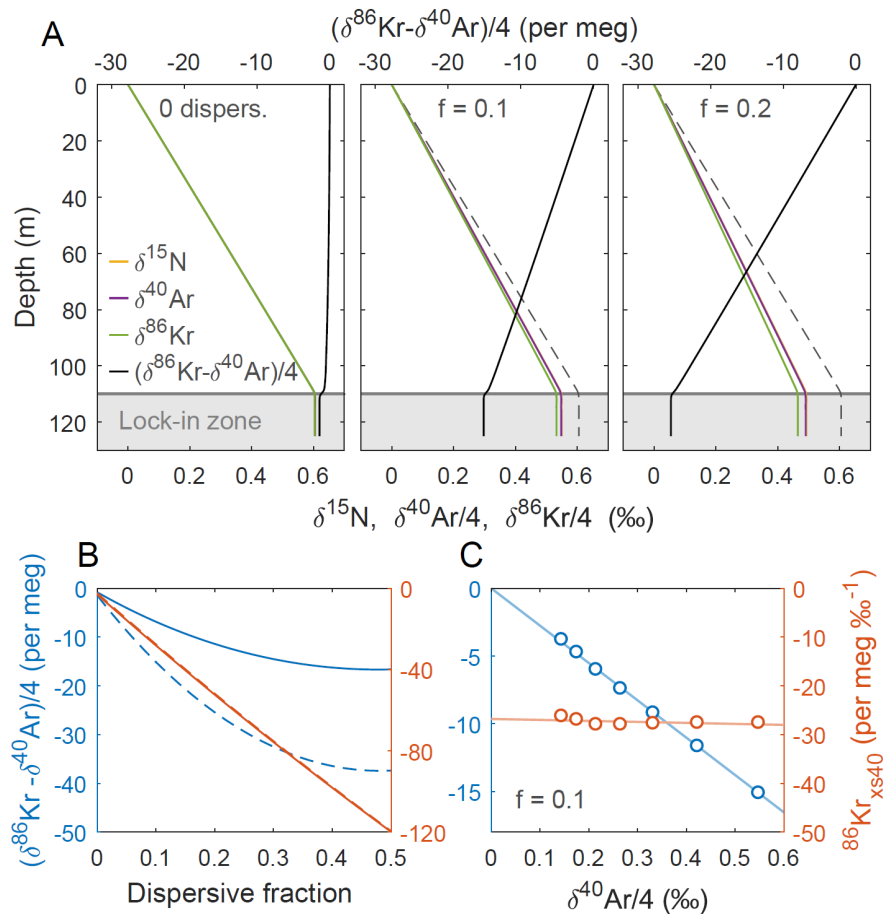
1188 Trenberth, K.E. (1991) Storm Tracks in the Southern Hemisphere. *Journal of the Atmospheric Sciences* 48, 2159-
1189 2178.

1190 Tudhope, A.W., Chilcott, C.P., McCulloch, M.T., Cook, E.R., Chappell, J., Ellam, R.M., Lea, D.W., Lough, J.M. and
1191 Shimmield, G.B. (2001) Variability in the El Niño-Southern Oscillation through a glacial-interglacial cycle.
1192 *Science* 291, 1511-1517.

1193 Wang, X., Auler, A.S., Edwards, R.L., Cheng, H., Ito, E., Wang, Y., Kong, X. and Solheid, M. (2007) Millennial-
1194 scale precipitation changes in southern Brazil over the past 90,000 years. *Geophys. Res. Lett.* 34.

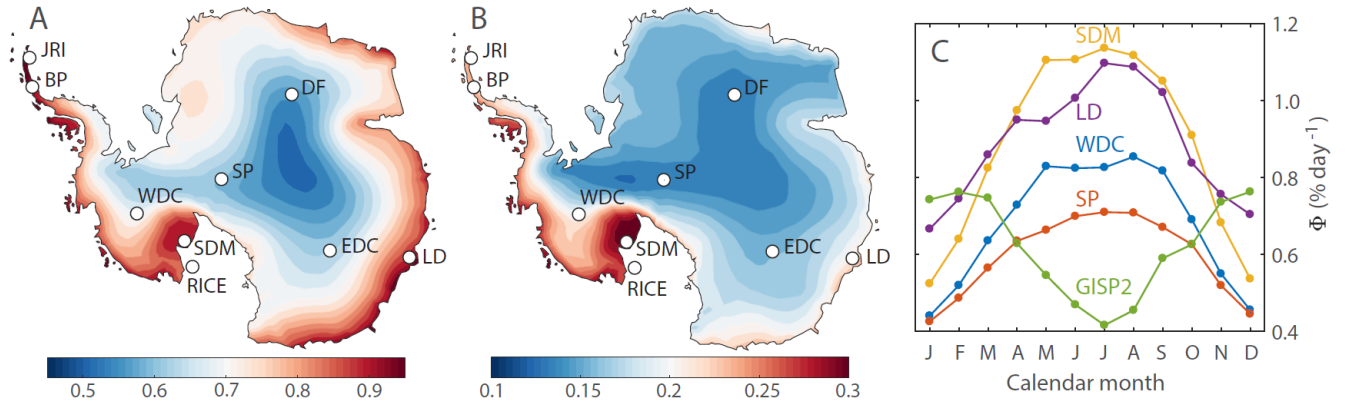
1195 Wang, Y.J., Cheng, H., Edwards, R.L., An, Z.S., Wu, J.Y., Shen, C.C. and Dorale, J.A. (2001) A High-Resolution
1196 Absolute-Dated Late Pleistocene Monsoon Record from Hulu Cave, China. *Science* 294, 2345-2348.

1197 Zheng, W., Braconnot, P., Guilyardi, E., Merkel, U. and Yu, Y. (2008) ENSO at 6ka and 21ka from ocean-atmosphere
1198 coupled model simulations. *Clim. Dyn.* 30, 745-762.



1199

1200 **Figure 1.** Idealized firn air transport model experiments of $^{86}\text{Kr}_{\text{xs}}$. Firn density is calculated using (Herron
 1201 and Langway, 1980), and the diffusivity using (Schwander, 1989). **A** Simulations using a fraction of
 1202 dispersive mixing of $f=0$ (left), $f=0.1$ (middle) and $f=0.2$ (right) for a hypothetical site with accumulation
 1203 rate of $A = 2 \text{ cm a}^{-1}$ ice equivalent and mean annual temperature $T = -60^\circ\text{C}$. At dispersive fraction f , effective
 1204 molecular diffusivity of all gases is multiplied by $(1-f)$ and dispersive mixing for all gases is set equal to f
 1205 times the effective molecular diffusivity of CO_2 . **B** Isotopic disequilibrium as a function of dispersive
 1206 mixing intensity at two different firn thicknesses of around 100 m (dashed, $A = 2 \text{ cm a}^{-1}$ and $T = -60^\circ\text{C}$) and
 1207 50 m (solid, $A = 2 \text{ cm a}^{-1}$ and $T = -43^\circ\text{C}$). We compare isotopic disequilibrium without (blue, left axis) and
 1208 with (orange, right axis) normalization. **C** Simulations at 10 % dispersive mixing, where each dot represents
 1209 different climatic conditions. Accumulation rate is $A = 2 \text{ cm a}^{-1}$ ice equivalent and mean annual temperature
 1210 is changed from -60°C to -30°C in steps of 5°C .



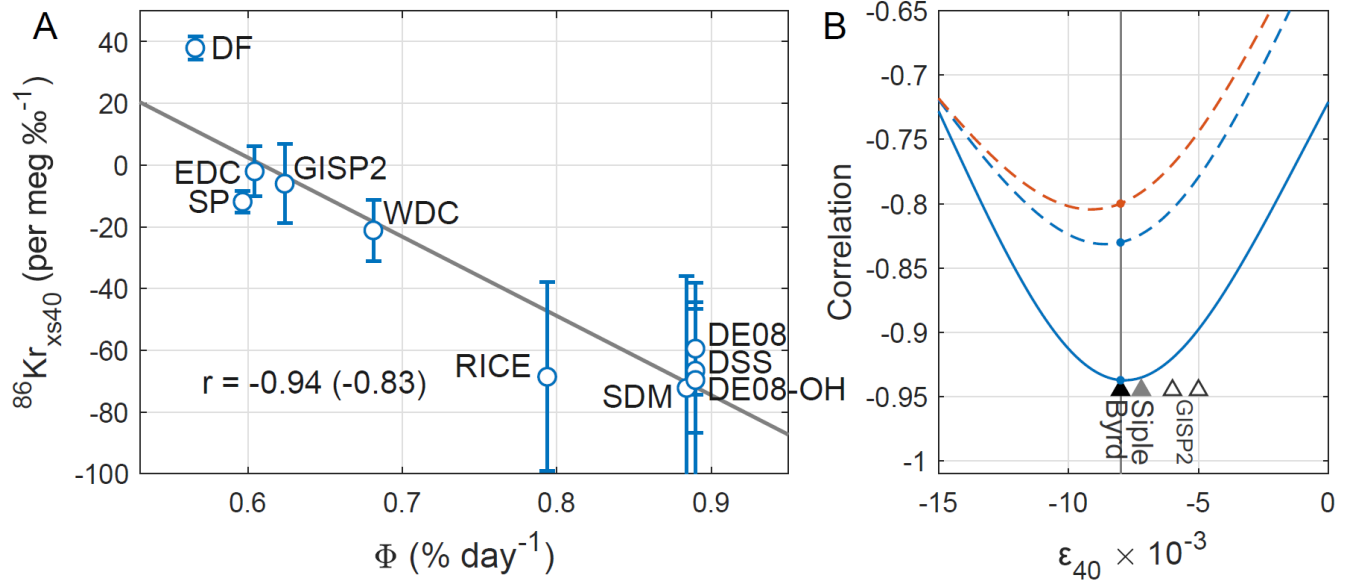
1211

1212

1213 **Figure 2.** Calibrating Kr-86 excess. **A** Annual-mean Φ in Antarctica over 1979-2017, in units of $\% \text{ day}^{-1}$.

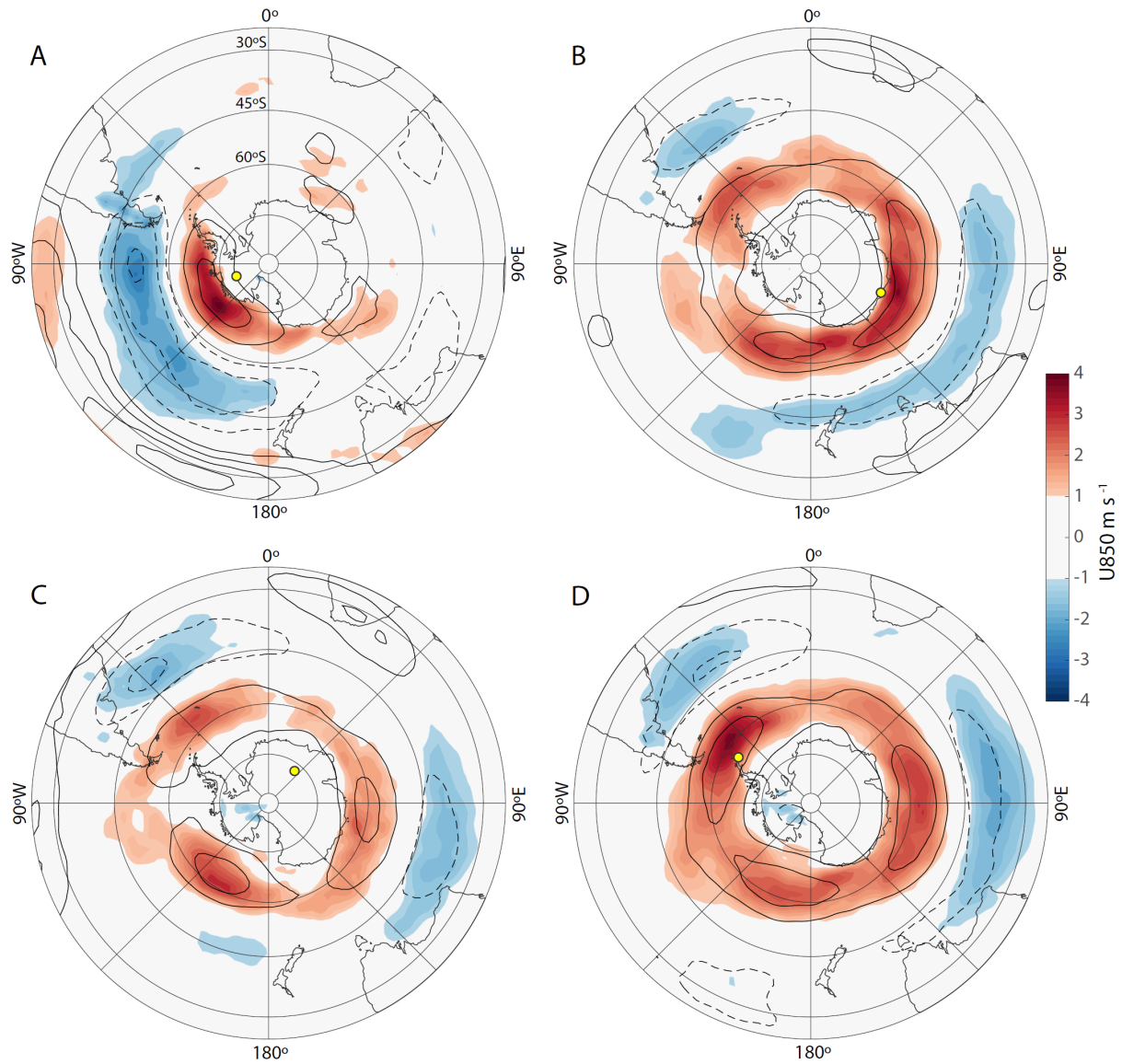
1214 **B** Interannual variability (1σ standard deviation) of annual-mean Φ over 1979-2017, in units of $\% \text{ day}^{-1}$. **C**

1215 Annual cycle in Φ for 1979-2017 for the indicated sites.



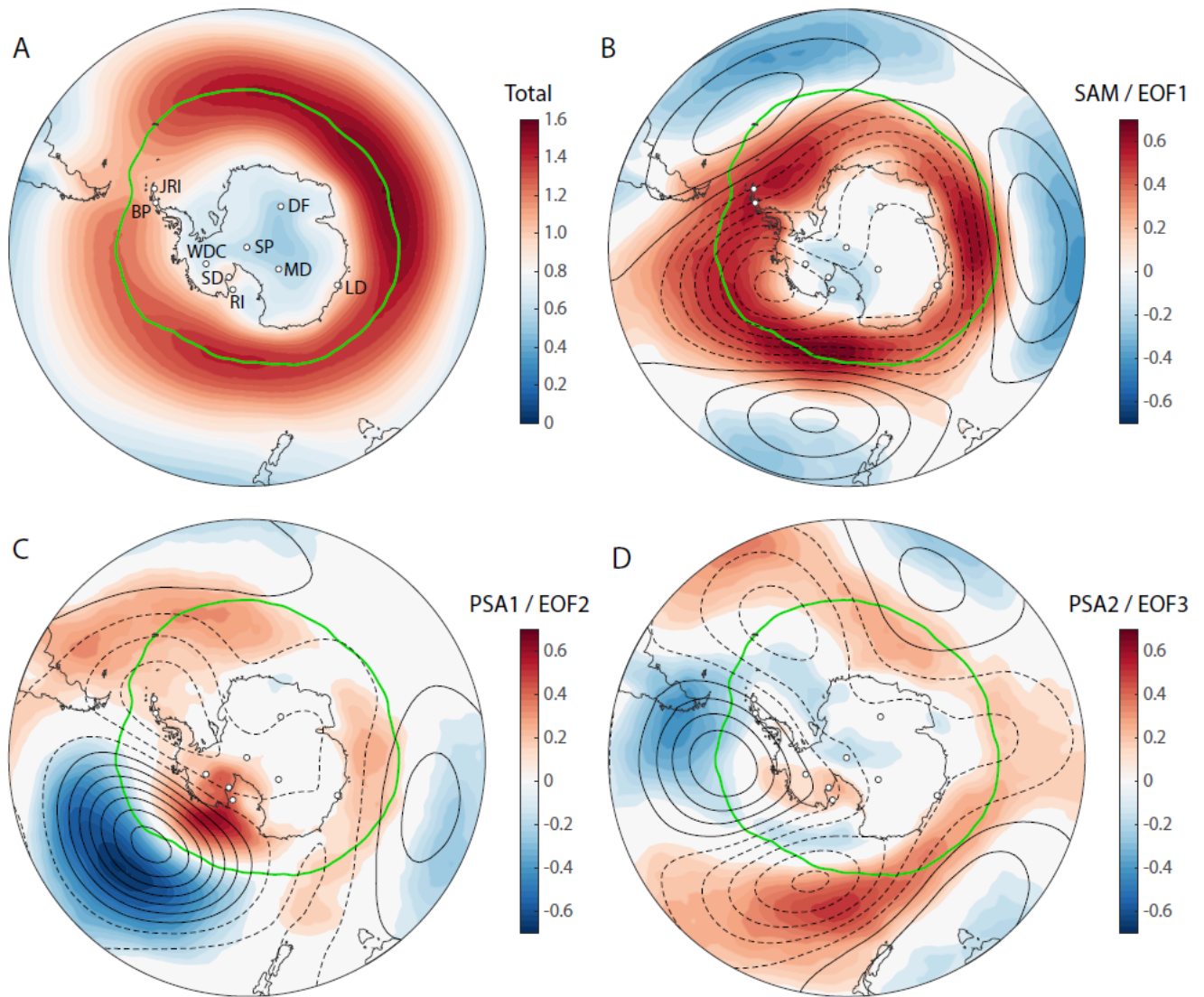
1216

1217 **Figure 3.** Calibrating Kr-86 excess. **A** $^{86}\text{Kr}_{\text{xs}}$ as a function of Φ for the calibration data set. Circles give the
 1218 site mean, and the error bars denote the $\pm 1\sigma$ standard deviation between samples (uncertainty in corrections
 1219 and measurements not included). The number of samples at each site is given in Table 1. Pearson correlation
 1220 coefficient is $r = -0.94$ when considering site data means and $r = -0.83$ when considering all individual
 1221 samples. Data are corrected for gas loss using $\epsilon_{40} = -0.008$ (Appendix A1), and corrected for thermal
 1222 fractionation using site-mean N-15 excess (Appendix A2). The calibration curve for $^{86}\text{Kr}_{\text{xs15}}$ is identical in
 1223 this case, with slightly larger errorbars. **B** Correlation of the calibration curve as a function of the gas loss
 1224 correction scaling parameter ϵ_{40} . The solid line gives the correlation for both site-mean $^{86}\text{Kr}_{\text{xs15}}$ and $^{86}\text{Kr}_{\text{xs40}}$
 1225 (identical); the dashed lines the correlation using individual samples for $^{86}\text{Kr}_{\text{xs40}}$ (blue) and $^{86}\text{Kr}_{\text{xs15}}$ (orange).
 1226 Triangles denote the ϵ_{40} estimate from the Byrd, Siple and GISP2 ice cores (Fig. A2; Kobashi et al., 2008a;
 1227 Severinghaus et al., 2003).



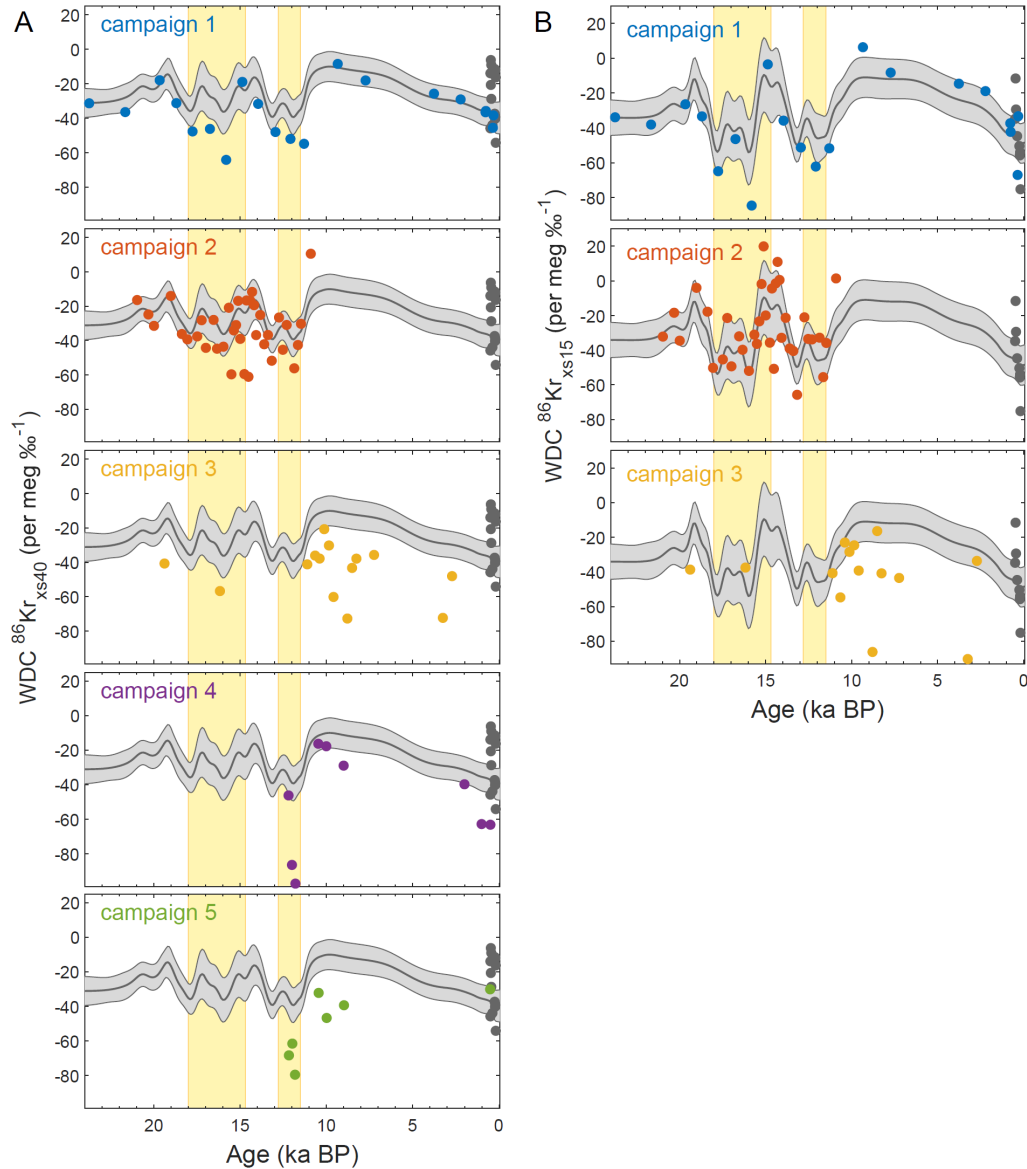
1228

1229 **Figure 4.** Zonal wind speed at 850 hPa (color shading, see scale bar) and 200 hPa (2 m s^{-1} contours)
 1230 regressed onto surface synoptic activity Φ at the Antarctic ice core sites of: **A** WAIS Divide; **B** Law
 1231 Dome (DE08, DE08-OH and DSSW20K); **C** Dome Fuji; **D** James Ross Island. Yellow dots mark the ice core
 1232 locations.



1233

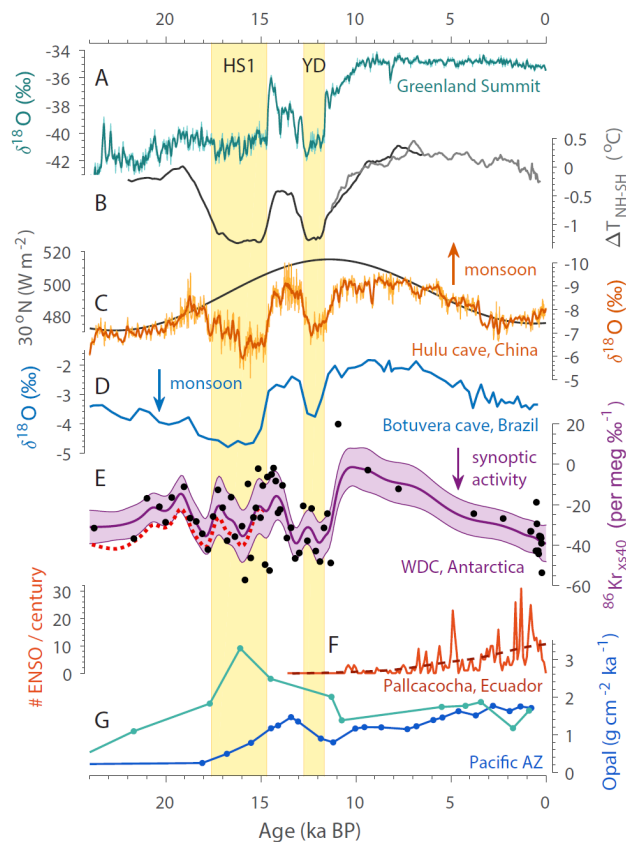
1234 **Figure 5.** Modes of SH extratropical atmospheric variability and their link to synoptic-scale surface
 1235 pressure variability in Antarctica. **A** Annual mean Φ in units of $\% \text{ day}^{-1}$. **B** Colors show correlation between
 1236 Φ and the Southern Annular Mode (SAM) index, with superimposed the 500 hPa geopotential height
 1237 anomalies in 10 m contours (positive contours solid, negative contours dashed). **C** as panel B, but for the
 1238 Pacific-South American Pattern 1 (PSA1). **D** As panel B, but for the Pacific-South American Pattern 2
 1239 (PSA2). SAM, PSA1 and PSA2 are defined as respectively the first, second and third EOFs (Empirical
 1240 Orthogonal Functions) of the 500 hPa geopotential height anomalies in 20° - 90° S monthly values in the
 1241 1979-2017 ERA interim reanalysis (Dee et al., 2011). In all panels the latitude of maximum Φ is denoted
 1242 by the green line.



1244

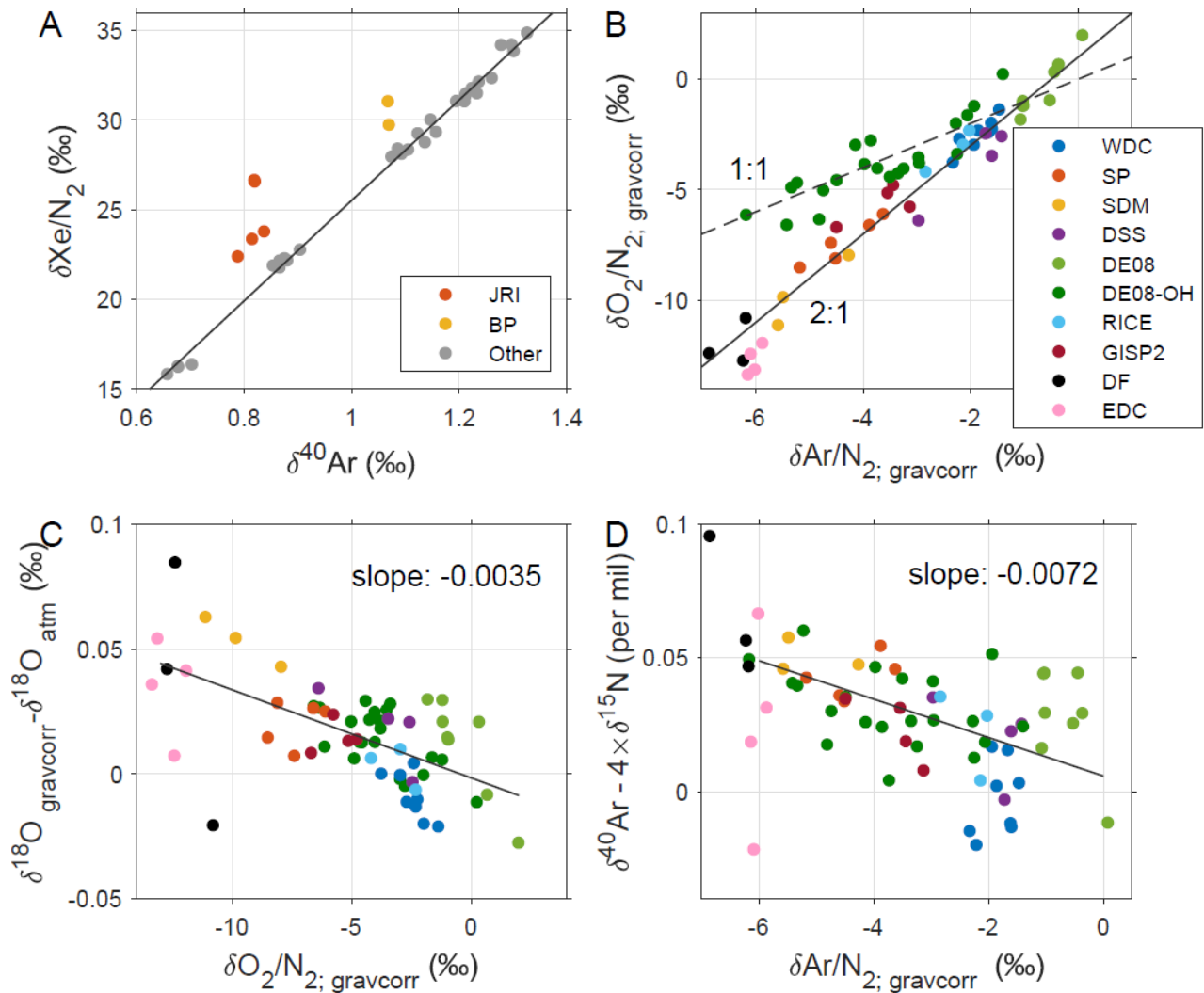
1245

1246 **Figure 6.** WAIS Divide Kr-86 excess records through the last deglaciation. **A** WDC $^{86}\text{Kr}_{\text{xs40}}$ data from the
 1247 five measurement campaigns. The gray curve shows a Gaussian smoothing curve to the combined data
 1248 from the first two campaigns; the light gray shaded area shows the $\pm 1\sigma$ uncertainty envelope based on a
 1249 10,000 iteration Monte-Carlo sampling of the errors and uncertainties. The WDC calibration data is shown
 1250 as gray circles for comparison. **B** As in panel (A), but for $^{86}\text{Kr}_{\text{xs15}}$. For campaigns 4 and 5 the sample was
 1251 not split, and no $\delta^{15}\text{N}$ data are available. The Heinrich Stadial 1 and Younger Dryas North-Atlantic cold
 1252 periods marked in yellow. Thermal corrections in the WDC $^{86}\text{Kr}_{\text{xs}}$ records are based on firm model
 1253 simulations.



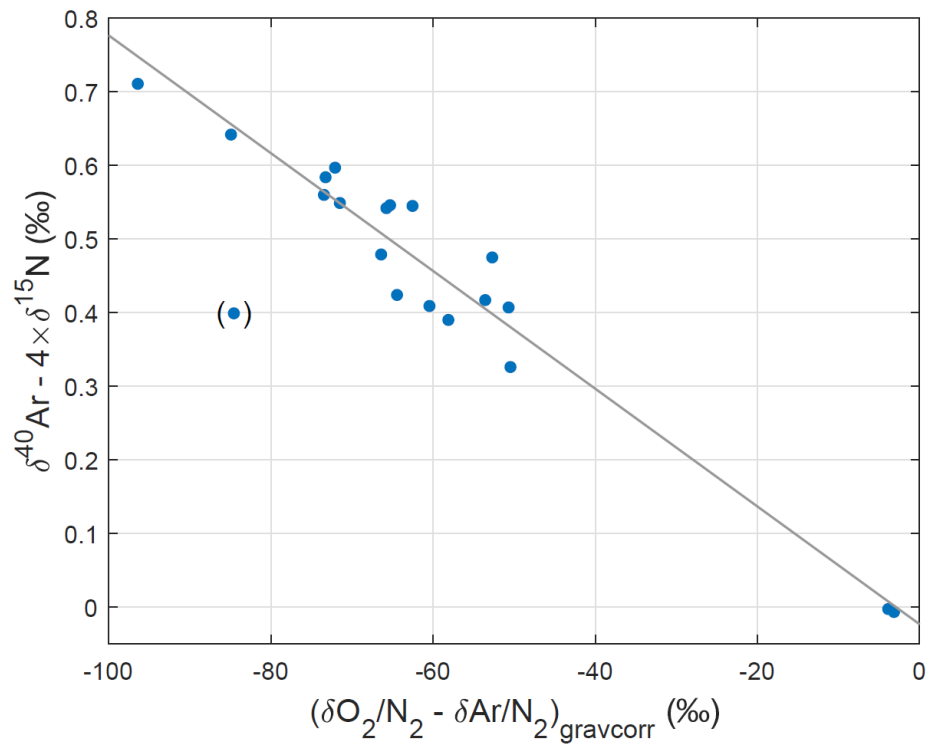
1255

1256 **Figure 7.** Climate records through the last deglaciation with the Heinrich Stadial 1 (HS1) and Younger
 1257 Dryas (YD) North-Atlantic cold periods marked in yellow. **A** Greenland Summit ice core stable water
 1258 isotope ratio $\delta^{18}\text{O}$ here the average of the GISP2 and GRIP ice cores (Grootes et al., 1993). **B** Hemispheric
 1259 temperature difference (McGee et al., 2014) based on global proxy compilations for the Holocene (Marcott
 1260 et al., 2013) and last deglaciation (Shakun et al., 2012). **C** Speleothem calcite $\delta^{18}\text{O}$ from Hulu and Dongge
 1261 Caves, China, as a proxy for East Asian summer monsoon strength (Dykoski et al., 2005; Wang et al.,
 1262 2001). Superimposed is summer solstice (June 21) insolation at 30°N . **D** Speleothem calcite $\delta^{18}\text{O}$ from
 1263 Botuvera cave, southern Brazil, as a proxy for South American summer monsoon strength (Cruz et al.,
 1264 2005; Wang et al., 2007). **E** Kr-86 excess record from WAIS Divide (this study); corrected for gas loss and
 1265 thermal fractionation (Appendix A). Center line and shaded envelope show the mean and $\pm 1\sigma$ uncertainty
 1266 interval of a 10,000 iteration Monte Carlo smoothing exercise (see text). The dotted red line equals the
 1267 center line with a correction for elevation change applied (Appendix A) using a simulated elevation history
 1268 (Golledge et al., 2014). **F** Number of El Niño events per century from laminations in sediments from Laguna
 1269 Pallcacocha, Ecuador (Moy et al., 2002). **G** Th-normalized opal flux in the Pacific Antarctic zone (south of
 1270 the polar front) from cores NBP9802-6PC1 (turquoise; 169.98°W , 61.88°S) and PS75/072-4 (blue;
 1271 151.22°W , 57.56°S), reflecting local productivity and (wind-driven) upwelling (Chase et al., 2003; Studer
 1272 et al., 2015). All isotope data in this figure are on the V-SMOW scale. Arrows show direction of increased
 1273 monsoon strength / synoptic activity.



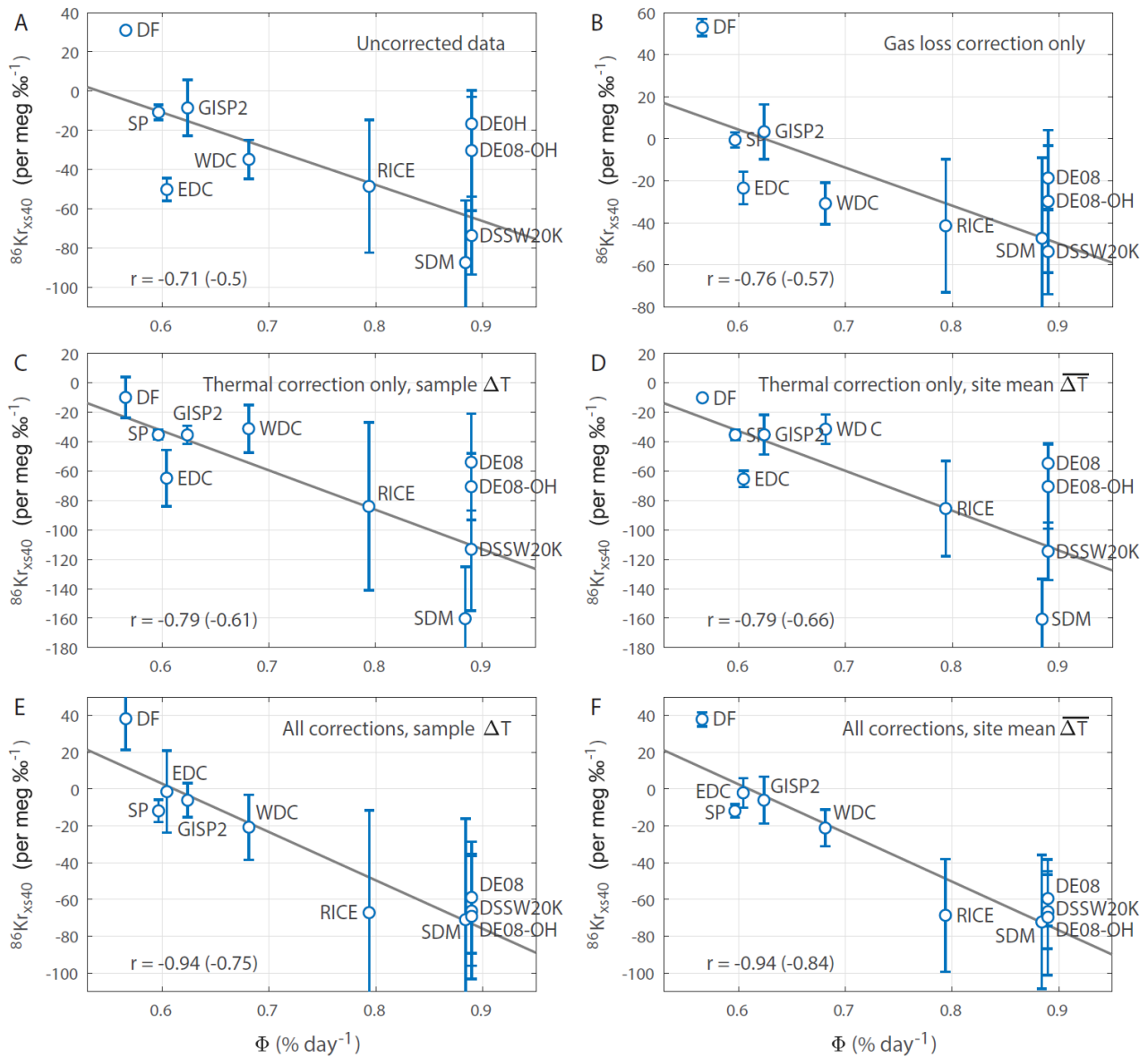
1274

1275 **Figure A1.** Elemental ratios in the 11-site calibration study of late Holocene samples. **A** $\delta\text{Xe}/\text{N}_2$ vs. $\delta^{40}\text{Ar}$
 1276 in all ice core samples. $\delta^{40}\text{Ar}$ is used solely to illustrate gravitational enrichment, and a similar picture arises
 1277 when plotted against any isotopic pair. Refrozen meltwater (elevated $\delta\text{Xe}/\text{N}_2$) was seen in all samples from
 1278 the Antarctic Peninsula (James Ross Island and Bruce Plateau sites), despite selecting samples free of
 1279 visible melt features. **B** The relationship between the commonly used gas loss proxies $\delta\text{O}_2/\text{N}_2$ and $\delta\text{Ar}/\text{N}_2$
 1280 corrected for gravity. **C** Enrichment in $\delta^{18}\text{O}$ (corrected for gravity and atmospheric $\delta^{18}\text{O}_{\text{atm}}$) plotted against
 1281 gravity-corrected $\delta\text{O}_2/\text{N}_2$ **D** $\delta^{40}\text{Ar}$ enrichment plotted against gravity-corrected $\delta\text{Ar}/\text{N}_2$. In all panels
 1282 gravitational correction is applied by subtracting $\delta^{15}\text{N}$ times the atomic mass unit difference.



1283

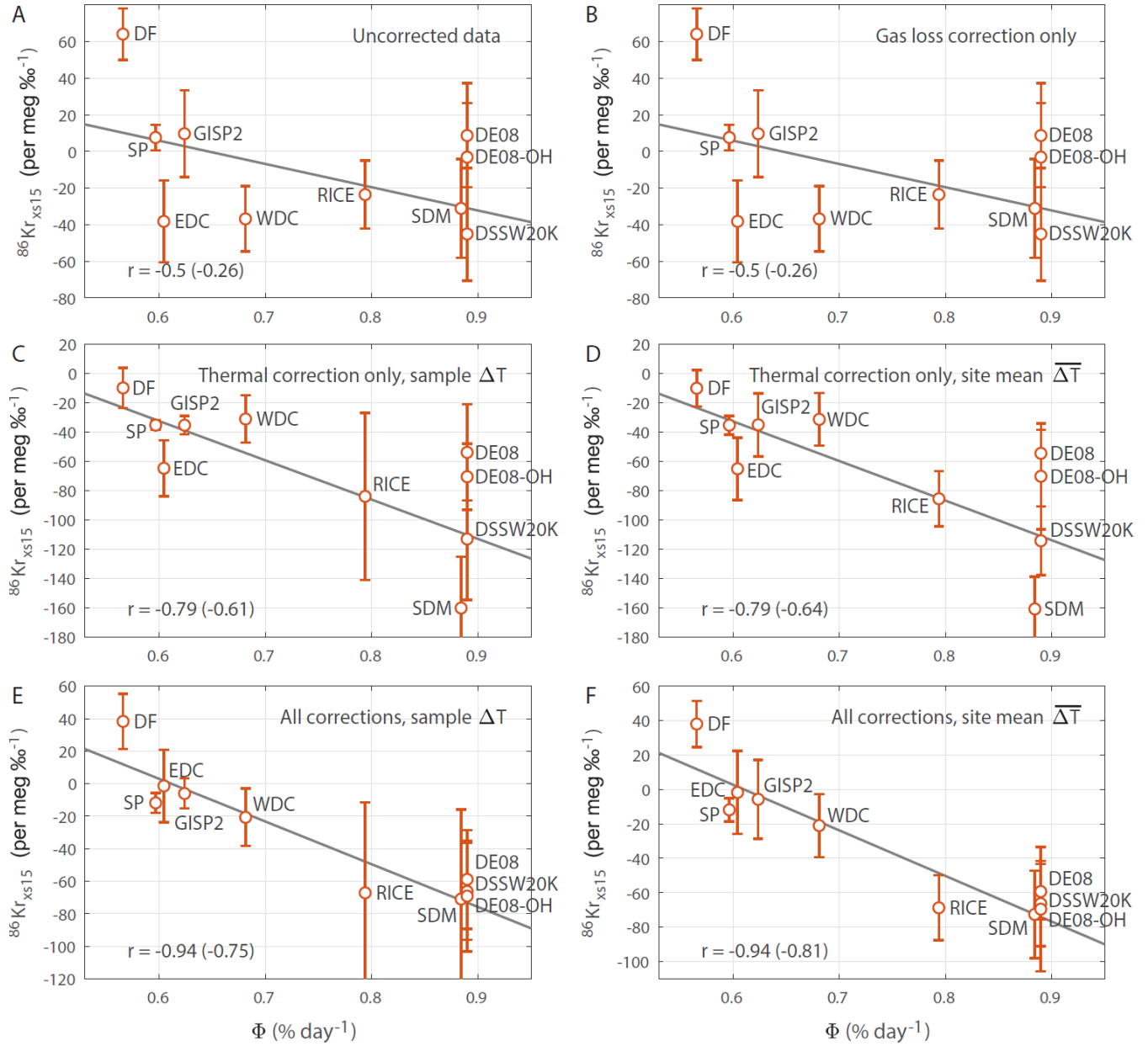
1284 **Figure A2.** Argon isotopic enrichment due to gas loss in the Byrd core used to determine the $\delta^{40}\text{Ar}$ gas loss
 1285 correction (appendix A1). The enrichment in $\delta^{40}\text{Ar}$ plotted as a function of gravitationally corrected $(\delta O_2/N_2$
 1286 $- \delta Ar/N_2)$ measured in the deep Antarctic Byrd ice core, which suffered heavy gas loss. Ice samples were
 1287 analyzed in the Bender Lab at the University of Rhode Island by Jeff Severinghaus in 1997. The slope of
 1288 the least-square fit is $\epsilon_{40} = -0.008$. The data point in parentheses is treated as an outlier and excluded
 1289 from the fitting.



1291

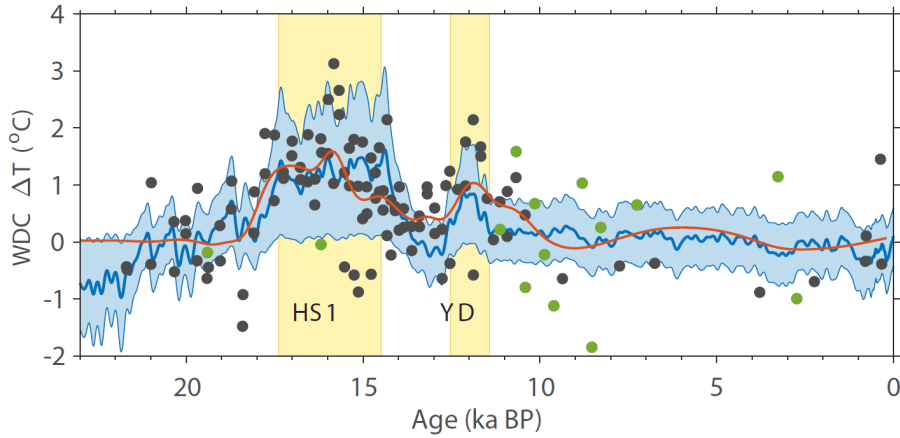
1292

1293 **Figure A3.** Influence of gas loss and thermal correction on the $^{86}\text{Kr}_{\text{xs}40}$ calibration. We plot $^{86}\text{Kr}_{\text{xs}40}$ as a
 1294 function of Φ **A** without any data corrections applied; **B** with only the gas loss correction applied ($\varepsilon_{40} =$
 1295 0.008); **C** with only the thermal correction applied using individual sample ΔT ; **D** with only the thermal
 1296 correction applied using individual site mean $\overline{\Delta T}$; **E** with both gas loss and thermal corrections applied
 1297 using individual sample ΔT ; **F** with both gas loss and thermal corrections applied using site mean $\overline{\Delta T}$. In
 1298 each panel the correlation to Φ are listed for the site-average and individual sample with the latter in
 1299 parentheses. For all correlations $p < 0.05$.



1300

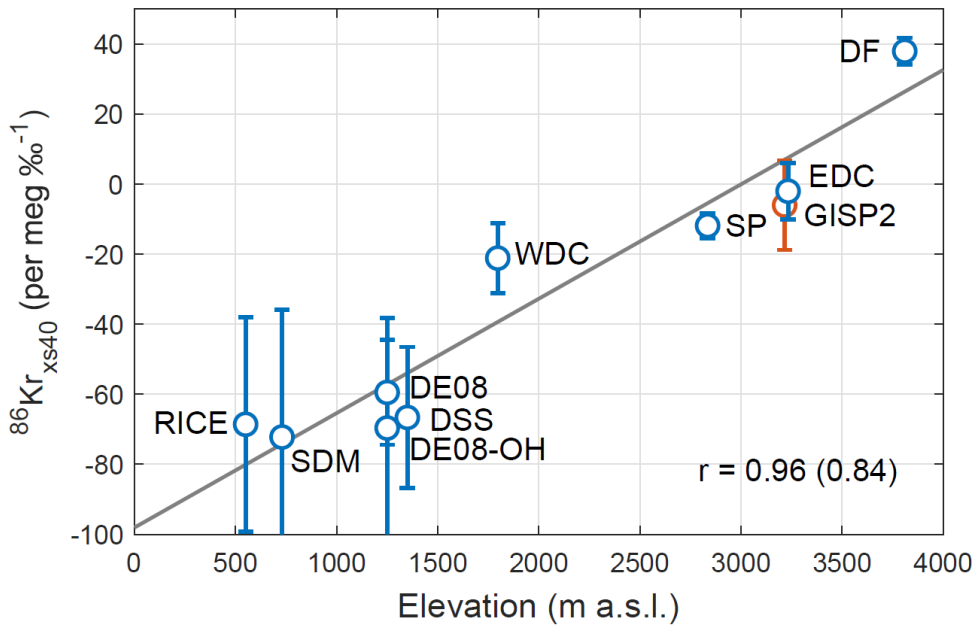
1301 **Figure A4.** Same as figure A3, but for $^{86}\text{Kr}_{\text{xs15}}$. Note that the gas loss correction (panel B) does not impact
 1302 $^{86}\text{Kr}_{\text{xs15}}$. For all correlations $p < 0.05$, except for panels A and B where $p = 0.16$ for the site-average
 1303 correlation.



1304

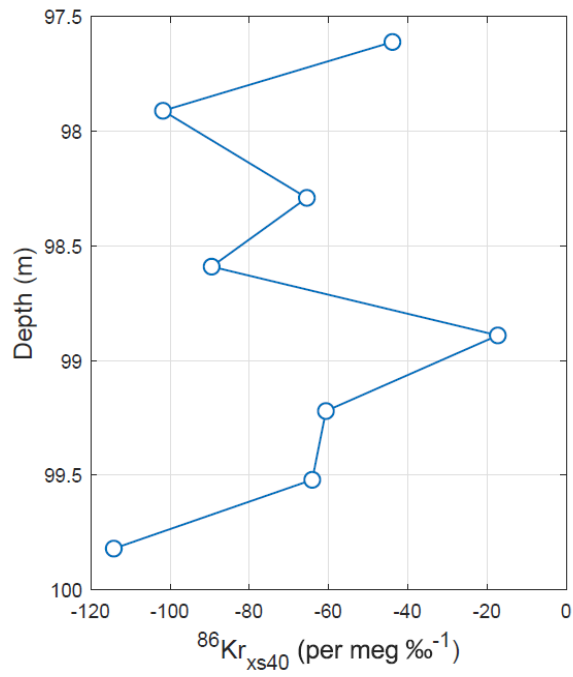
1305 **Figure A5.** The ΔT correction applied to the downcore records. Blue envelope shows the $\pm 2\sigma$ range of
 1306 thermal correction scenarios in the Monte Carlo sampling, together with the mean (blue line). Gray dots
 1307 show WDC ΔT estimates from available ^{15}N -excess data, with the red curve being a Gaussian smoothing
 1308 function to the data. Green dots are ^{15}N -excess from campaign 3, showing somewhat greater scatter.

1309



1310

1311 **Figure A6.** Kr-86 excess dependence on site elevation. Vertical axis is the $^{86}\text{Kr}_{\text{xs}}$. The linear fit has a slope
 1312 of 34 per meg ‰^{-1} per 1000 m elevation.



1313

1314 **Figure B1** High-resolution sub-annual sampling of $^{86}\text{Kr}_{\text{xs40}}$ in the DE08-OH site. The annual layer thickness
 1315 at this depth is around 1.3 m.

1316 **Table 1.** Ice core sites used in this study, with N the number of samples included in the calibration study.
 1317 See the main text for acronyms.
 1318

Site	T (°C)	A (m ice a ⁻¹)	Φ (% day ⁻¹)	Latitude	Longitude	N
WDC	-31	0.22	0.68	79.5°S	112.1°W	8 ^a
DF	-57	0.028	0.56	77.3°S	39.7°E	3
SP	-51	0.078	0.6	90.0°S	98.2°W	5
SDM	-25	0.13	0.88	81.7°S	149.1°W	3
DSSW20K	-21	0.16	0.89	66.8°S	112.6°E	4
DE08	-19	1.2	0.89	66.7°S	113.2°E	8
DE08-OH	-19	1.2	0.89	66.7°S	113.2°E	8 ^b
RICE	-24	0.24	0.79	79.4°S	161.7°W	3 ^a
EDC	-55	0.03	0.6	75.1°S	123.4°E	4
JRI	-14	0.68	0.97	64.2°S	57.7°W	5 ^c
BRP	-15	2	0.9	66.1°S	64.1°W	2 ^c
GISP2	-32	0.23	0.62	72.6°N	38.5°W	4

1319 ^a Not including one sample rejected due to technical problems.

1320 ^b Only shallow samples due to strong gas loss in deeper samples attributed to warm storage conditions.

1321 ^c Refrozen meltwater present as indicated by elevated Xe/N₂ ratio.

1322
 1323
 1324
 1325

1326 **Table 2.** Pearson correlation between Φ at the ice coring sites and large-scale atmospheric circulation.
 1327 Correlations are calculated using annual mean data (all months, April-March). We only list the
 1328 statistically significant correlations ($p < 0.1$). The Niño 3.4 is calculated over 5°S - 5°N, 190°E - 240°E,
 1329 using SST from Huang et al. (2014); the PDO index is from Mantua and Hare (2002).
 1330

Site	SAM	PSA1	PSA2	Niño 3.4	PDO	Sea ice Am-Bell	Sea ice Ross
WDC	-	0.31	-	0.31	0.28	-	-
SDM	-	0.47	0.34	0.43	0.45	-	-0.32
RICE	-	0.41	0.34	0.34	0.45	-	-0.30
SP	-	-	-0.32	-	-0.30	-	-
LD	0.45	-	-	-	-	-	-
DF	0.37	-	-	-	-	-	-
EDC	0.30	-	-	-	-	-	-
JRI	0.67	-	-	-	-	0.31	-
BRP	0.68	-	-	-	-	-	-

1331
 1332
 1333